Supporting Information file… …

An Alkyne Linchpin Strategy for Drug:Pharmacophore Conjugation: Experimental and Computational Realization of a *meta*-selective Inverse Sonogashira Coupling

Sandip Porey,[1,†] Xinglong Zhang,[2,†] Suman Bhowmick,[1] Vikas Kumar Singh,[1] Srimanta Guin,[1,*] Robert S. Paton,[2,3,*] and Debabrata Maiti[1,*]

[1] Department of Chemistry, Indian Institute of Technology Bombay, Powai, Mumbai 400076, India

[2] Chemistry Research Laboratory, University of Oxford, Mansfield Road, Oxford, OX1 3TA, UK

[3] Department of Chemistry, Colorado State University, Fort Collins, Colorado 80523, USA

[†] These authors contributed equally to this work

Email: dmaiti@iitb.ac.in (DM)
Email: robert.paton@colostate.edu (RSP)
Email: srgnchem@gmail.com (SG)

2.6. Computational methods

Density functional theory (DFT) calculations were performed with Gaussian 16 rev. A.03.[8] Geometry optimisations were carried out using recently developed global-hybrid meta-NGA (nonseparable gradient approximation) MN15 functional[9] with a mixed Karlsruhe-family basis set of triple-ζ valence def2-TZVPPD (where 'D' indicates diffuse basis functions) for Br[10], Pd[10,11] and Ag[10,11] atoms and def2-SVP[12,13] for all other atoms (BS1). This functional was chosen as it performs much better than many other functionals (e.g. ωB97X-D and TPSS) in predicting transition metal (TM) reaction barrier heights and better geometry for both TM complexes and organic molecules.[9] MN15 has also been employed to study similar Pd-catalytic systems with excellent agreement with experimental results.[14–19] Minima and transition structures on the potential energy surface (PES) were confirmed as such by harmonic frequency analysis, showing respectively zero and one imaginary frequency, at the same level of theory. Where appropriate, intrinsic reaction coordinate (IRC) analyses[20,21] were performed to confirm that the said TSs connect to the right reactants and products. Single point (SP) corrections were performed separately with either MN15 or ωB97X-D[22] functional and def2-QZVPP[12] basis set for all atoms. The SMD continuum solvation model[23] was used to include the effect of 1,4-dioxane solvent on the computed Gibbs energy profile. Gibbs energies were evaluated at the reaction temperature of 353.15 K, using a quasi-RRHO treatment of vibrational entropies.[24,25] Vibrational entropies of frequencies below 100 cm^{-1} were obtained according to a free rotor description, using a smooth damping function to interpolate between the two limiting descriptions. The free energies were further corrected using standard concentration of 1 mol/L, which were used in solvation calculations. SMD(1,4-dioxane)-ωB97X-D/def2-QZVPP//MN15/BS1 Gibbs energies were given with SMD(1,4-dioxane)-MN15/def2-QZVPP//MN15/BS1 Gibbs energies given in brackets throughout. Unless otherwise stated, the former set of Gibbs energy values are used for discussion. All Gibbs energy values in the text and figures are quoted in kcal mol^{-1} throughout.

Non-covalent interactions (NCIs) were analysed using NCIPLOT[26] calculations. The .wfn files for NCIPLOT were generated at MN15/DGDZVP[27,28] level of theory. NCI indices calculated with NCIPLOT were visualised at a gradient isosurface value of s = 0.5 au. These are coloured according to the sign of the second eigenvalue (λ_2) of the Laplacian of the density ($\nabla^2\rho$) over the range of -0.1 (blue = attractive) to +0.1 (red = repulsive). Molecular orbitals are visualised using an isosurface value of 0.05 throughout. All molecular structures and molecular orbitals were visualized using PyMOL software.[29] Geometries of all optimized structures (in .xyz format with their associated energy in Hartrees) are included in a separate folder named alkynylation_structures_xyz with an associated README file. All these data have been deposited with this Supporting Information and uploaded to zenodo.org (DOI:10.5281/zenodo.3376707). All Python scripts used for data analysis have been made available - https://github.com/bobbypaton - under a creative commons CC-BY license.

2.6.1 Conformational considerations for starting materials

The starting material for computational modelling, sulfonyl arene, 1a, was first conformationally sampled. The possible rotamers for sulfonyl arene, 1a, were generated by systematically varying a combination of key dihedral angles shown in red (Scheme S1) and optimising the structures. The lowest energy conformer was used for subsequent calculations.

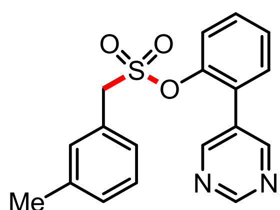

1a

Scheme S1. Rotamers were generated by varying the dihedral angles in red in conformational sampling of the most stable conformer used for reaction modelling.

2.6.2 Frontier molecular orbitals (FMOs) of starting materials

Figure S5 shows the FMOs for the starting material bromoethynyltrimethylsilane **1b** (hereafter bromoalkyne) and ethynyltrimethylsilane **1c** (hereafter TMS-alkyne). In **1b**, the HOMO arises predominantly from the π-electrons from the alkyne triple bond. This electron-rich π-bond can be donated to a vacant d-orbital on the electrophilic Pd(II) centre, giving rise to π-complexes with the transition metal before further transformations. Interestingly, the LUMO of **1b** is σ^*_{CBr} instead of π^*_{CC}. These have implications on the reactivity of bromoalkyne **1b**, suggesting that oxidative insertion of **1b** breaking the C–Br bond could be possible.

However, it seems that **1b** acts predominantly as a *π*-donor rather than *π*-acceptor, as seen in the HOMO for both oxidative insertion and 1,2-migratory insertion of **1b**, where the major contribution comes from the *π*-electrons from the alkyne triple bond (Figure S8). FMOs for TMS-alkyne **1c** are also shown in Figure S5. The HOMO is π_{CC} and the LUMO is π^{*}_{CC}. These are rather different from FMOs in **1b**, implicating different reactivity (see section 2.6.10 for a discussion of the reactivity with **1c** as a substrate).

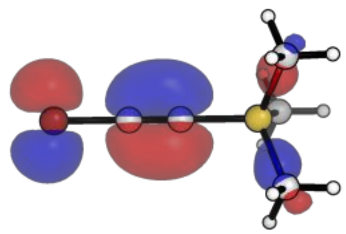	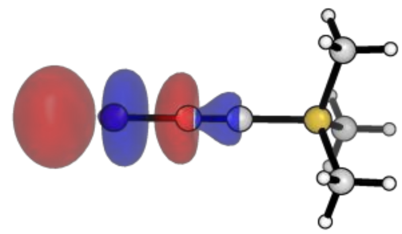
HOMO of 1b	**LUMO of 1b**
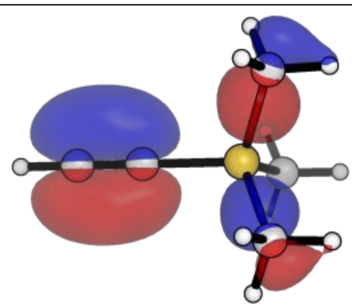	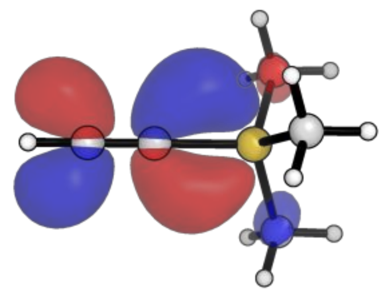
HOMO of 1c	**LUMO of 1c**

Figure S5. FMOs for bromoethynyltrimethylsilane **1b** and ethynyltrimethylsilane **1c** at an isosurface value of 0.05.

2.6.3 C–H activation in the presence and the absence of ligand

The full energy profile for the reaction is given in Figure S6, with key optimised geometries. For the C–H activation step, in the absence of the absence of mono-protected amino acid (MPAA) ligand, *N*-acetylglycine, the reaction has a high barrier of 28.0 kcal mol-1. In the presence of the ligand, the TS is lowered in activation barrier by forming a [5,6]-membered palladacyle (**ts-1'** at $19.7^{\ddagger}$ ($20.9^{\ddagger}$) kcal mol^{-1}). Other possible arrangements of this ligand, following ref.[10], were found to have higher activation barriers than **ts-1'** (Scheme S2) and are thus not competitive.

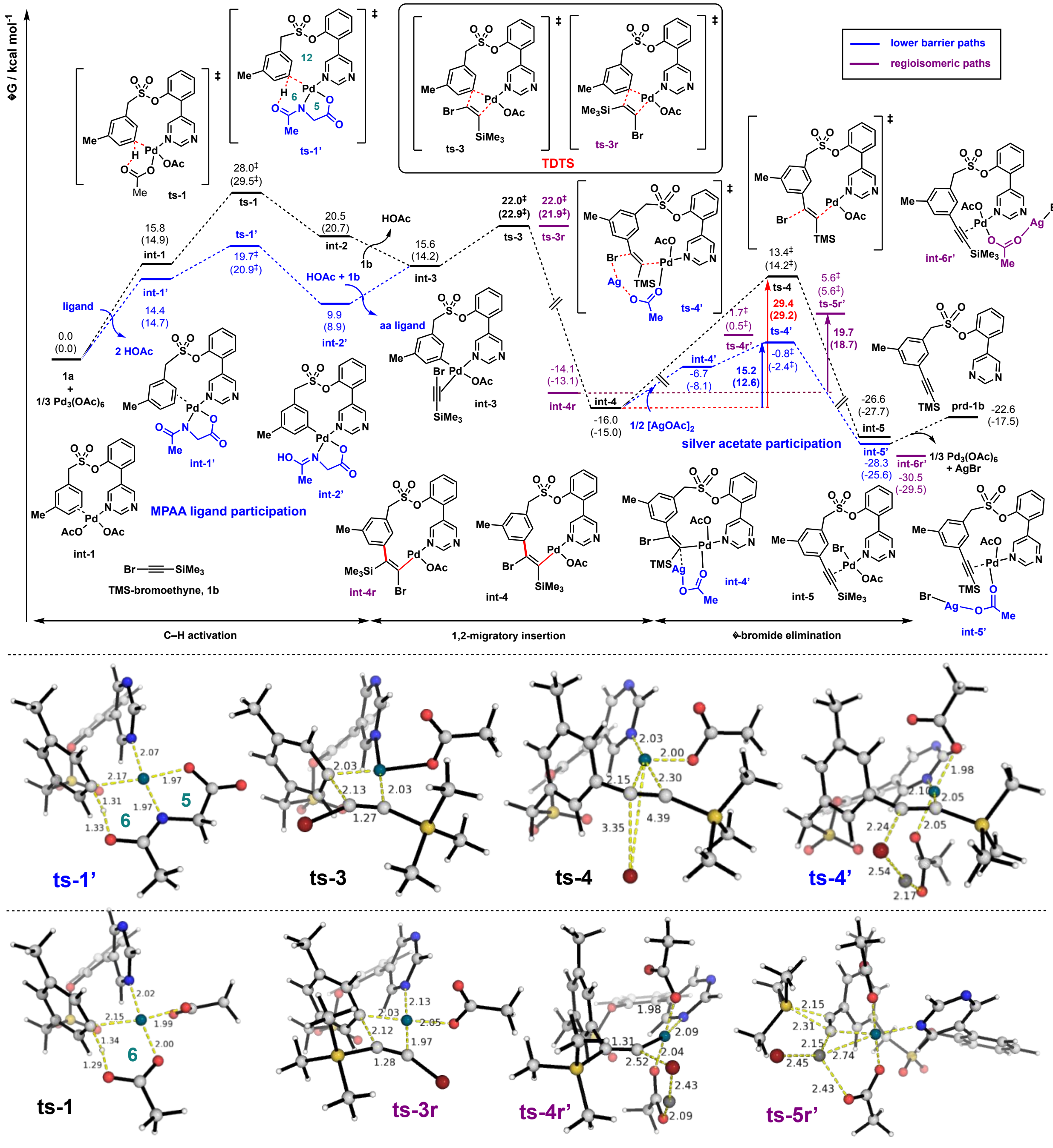

Figure S6. Full Gibbs energy profile for the reaction and selected optimized TS strucutres.

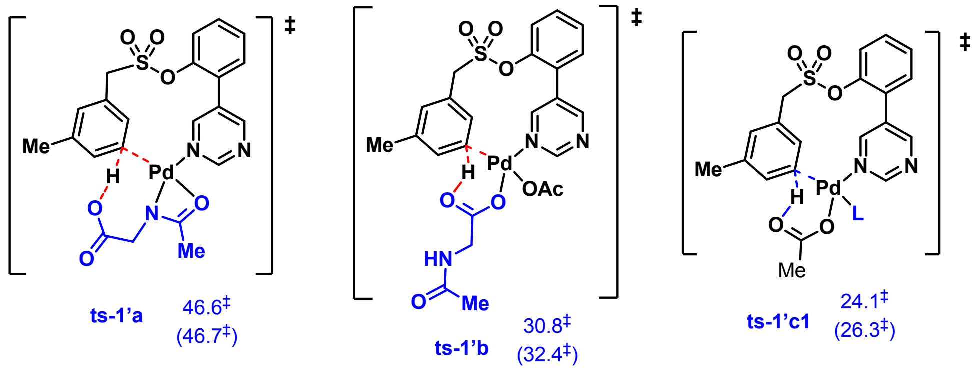

Scheme S2. Other possible arrangements of the ligand for C–H activation step.

2.6.4 Replacement of a.a. ligand by acetate ligand in migratory insertion step

The turnover frequency-determining transition state (TDTS) for the reaction is the 1,2-migratory insertion of bromoalkyne. We investigated the effect of using acetate ligand in replacement of the amino acid (a.a.) ligand for this step since all these forms have the generic form shown in Scheme S3(e) with variable R–group. We note that the energies are rather close (Scheme S3), without complete conformational sampling. Following the approach adopted in ref.[19] where complete conformational samplings were performed, showing that using acetate ligand instead of full a.a. ligand for this step does not affect the overall energy profile, we used, for simplicity, acetate ligand for the modelling of all steps subsequent to C–H activation. The a.a. ligand’s main role in this reaction is to lower the C–H activation barrier significantly, making this step reversible. Its subsequent coordination to Pd-center is monodentate in fashion, similar to the coordination mode of acetate ligand. This Pd–N interactions would dominate over other possible non-covalent interactions (or unfavorable sterics) in the side chains.

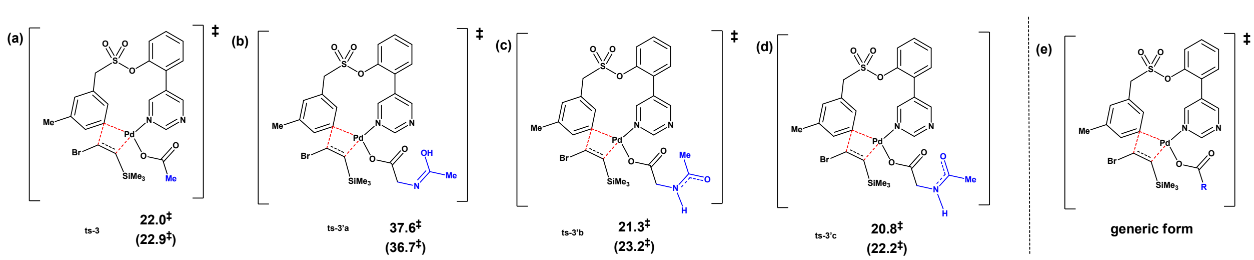

Scheme S3. Comparison of rate-determining 1,2-migratory insertion step using different ligands.

2.6.5 Alternative mechanism: oxidative addition of bromoethynyltrimethylsilane 1b

The oxidative addition (OA) of bromoethynyltrimethylsilane **1b** was investigated as Pd(II) were known to cycle through Pd(II)/Pd(IV) manifold.[30] All possible arrangements of OA of **1b** were investigated (Figure S7). These all have activation barriers > 40 kcal mol^{-1}, making this mechanistic path inaccessible; the alternative path of 1,2-migratory insertion, as discussed in the main text, with a barrier of 22.0 kcal mol^{-1}, is much more feasible.

ts-3-oa-c1	**ts-3-oa-c2**
42.5‡ (41.8‡)	45.5‡ (44.9‡)
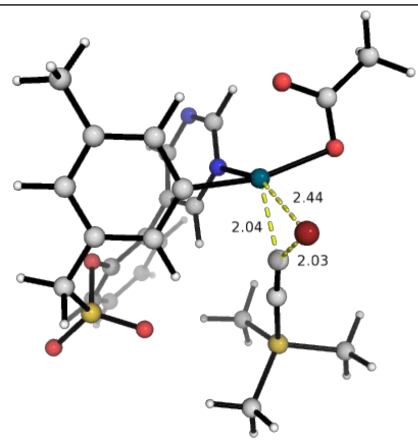	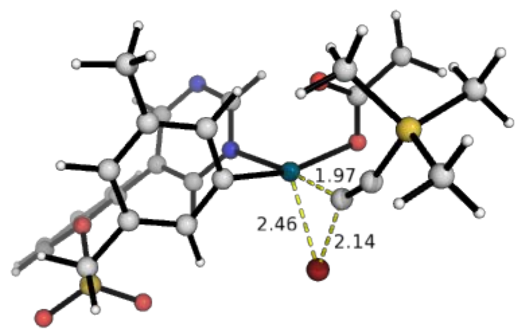
ts-3-oa-c3	**ts-3-oa-c4**
46.6‡ (45.5‡)	48.1‡ (47.5‡)
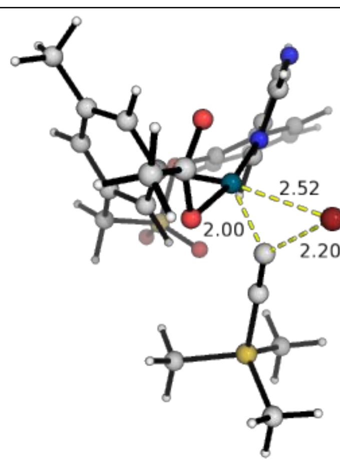	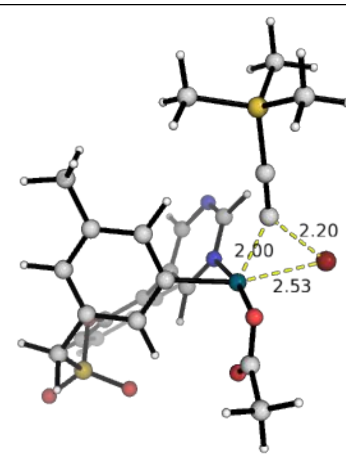

Figure S7. Oxidative addition of bromoethynyltrimethylsilane 1b.

2.6.6 Conformers for 1,2-migratory insertion and β-bromide elimination

Transition state (TS) conformers for 1,2-migratory insertion and β-bromide elimination are shown in Figure S8. These differ in the orientations of the acetate ligand and the side in which β-bromide elimination occurs. They are found to be very close in energy, indicating that the conformational flexibility in the ligand does not change the TS energies very much.

<table>
<tr><th>ts-3</th><th>ts-3-c2</th></tr>
<tr><td>22.0‡ (22.9‡)</td><td>22.1‡ (23.1‡)</td></tr>
<tr><td>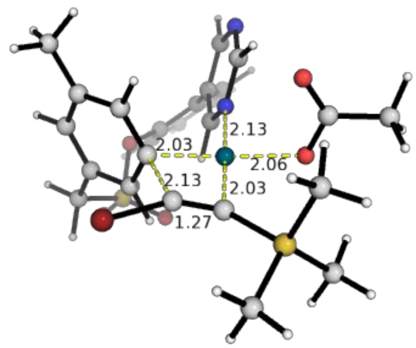
</td><td>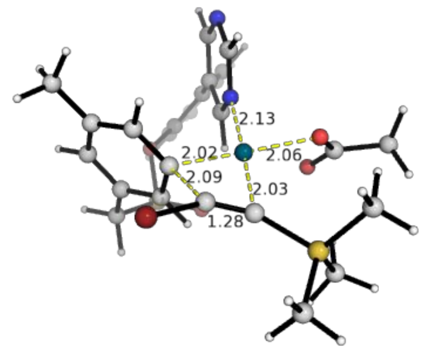
</td></tr>
<tr><th>ts-4</th><th>ts-4-c2</th></tr>
<tr><td>13.4‡ (14.2‡)</td><td>13.3‡ (13.1‡)</td></tr>
<tr><td>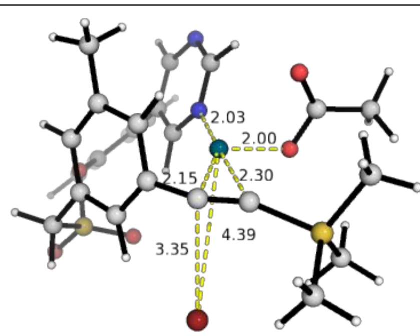
</td><td>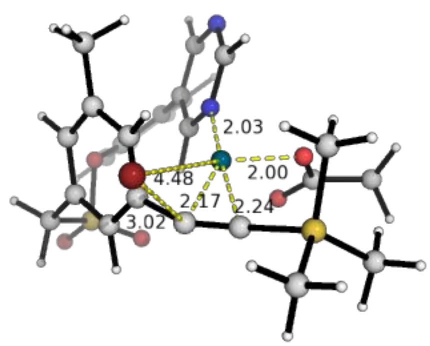
</td></tr>
</table>

Figure S8. Optimised geometries for 1,2-migratory insertion and β-bromide elimination transition state conformers.

2.6.7 Role of silver acetate additive

Silver carboxylate salts are commonly employed as additives in Pd-catalysed C–H activation.[31–35] In many systems, silver salt plays an essential role in enhancing the reaction rate and/or yields. Various roles of silver carboxylate AgCOOR salts in such reactions have been proposed: (1) they serve as a source of carboxylate for the Pd(II) metal-centre, participating in carboxylate-assisted concerted metalation deprotonation (CMD) in the C–H activation step;[35-39] (2) they act as a terminal oxidant to regenerate Pd(II) catalyst;[40–42] (3) they form heterometallic Pd−Ag complexes that facilitate C−H activation;[40,43,44] (4) they directly activate C−H bond forming Ag–C intermediate;[45,46] (5) they act as halide scavengers in PdX (X = halide) complex after the reductive elimination step.[47] The experimental work to establish the exact role of these silver additives are rare and an understanding of their exact roles in the mechanistic picture is rather incomplete.

Silver carboxylates are known to exist in dimeric form.[47–50] We computed the energy differences in the thermodynamic stabilities of both the monomeric and dimeric form of silver acetate and found that the dimeric form $[AgOAc]_2$ is more stable; the formation of $[AgOAc]_2$ from AgOAc monomers is -16.7 (-19.9) kcal mol^{-1} downhill. This enhanced stability in the dimer has been attributed to Ag–Ag interactions.[35,49] The more stable dimer (or in fact, ½ $[AgOAc]_2$) is used in the Gibbs energy calculations of silver additive participation throughout (the use of AgOAc monomer would artificially lower the activation barrier of **ts-4'** since AgOAc monomer is already high in energy).

In the absence of silver salt, the β-bromide elimination step has a very high activation barrier (**ts-4**, 29.4 kcal mol^{-1}, Figure S6). For the present transformation, silver cation plays a role in assisting β-bromide elimination step by forming silver bromide salt. An initial TS search placing the Ag^+ ion adjacent to the leaving Br^- as the former pulls off the latter yielded a TS that is higher in activation barrier than that without silver acetate (Figure S9, **ts-4'z**); only in **ts-4'** where not only Ag^+ interacts with the leaving Br^- but also the acetate coordinates to Pd(II) was the transition state lower in activation barrier. In the presence of silver acetate, the HOMO shows that there is predominant electron donation from bromoalkyne π-electrons to the vacant d-orbital on Pd(II) centre, this enhanced interaction is favourable to product formation as the bromide ion leaves (Figure S9). Although there seems to be more steric strain due to non-covalent interactions (NCIs) in **ts-4’**, the formation of Ag–Br bond is enthalpically favoured and more dominant over NCIs, thus lowering the activation barrier of this transition state.

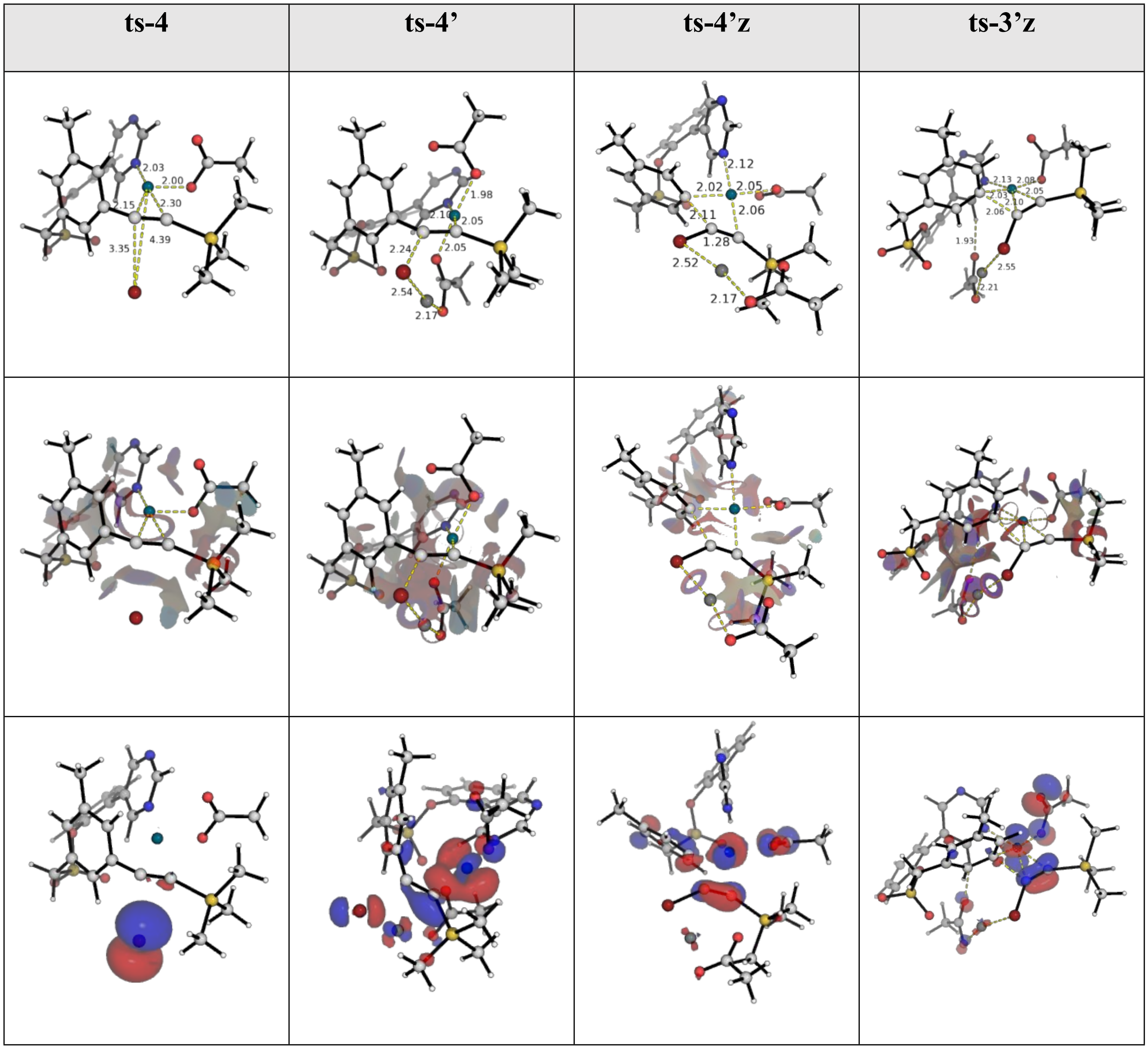

Figure S9. Optimised structures, NCI plots and HOMOs for β-bromide elimination without (**ts-4**) and with (**ts-4’** and **ts-4’z**) silver acetate co-ligand and for 1,2-migratory insertion with silver acetate co-ligand (**ts-3’z**).

For completeness, we went further to ascertain the role, if any, of silver acetate in affecting the 1,2-migratory insertion step. We found that, introducing AgOAc (**ts-3’z**) increased the activation barrier to 40.0 kcal mol^{-1}, which is much higher than **ts-3** without any AgOAc participation at 22.0 kcal mol^{-1}. The acetate ligand from silver could not coordinate to Pd-centre (despite the initial geometry guess as so) in the optimised structure as Pd(II) is tetra-coordinating and all coordination sites have been occupied (Figure S9).

2.6.8 Regioselectivity in 1,2-migratory insertion of bromoethynyltrimethylsilane 1b

Figure S10 shows the energy profile for the regioconvergent formation of alkynylated product. All activation barriers are thermally accessible at the reaction temperature of 80ºC. TS structures are shown in Figure S11.

It was found that the regioisomeric 1,2-migratory insertions of **1b** (**ts-3** and **ts-3r**, Figure S10) have almost identical barrier, at 22.0 kcal mol^{-1}, suggesting unselective 1,2-migatory insertion.

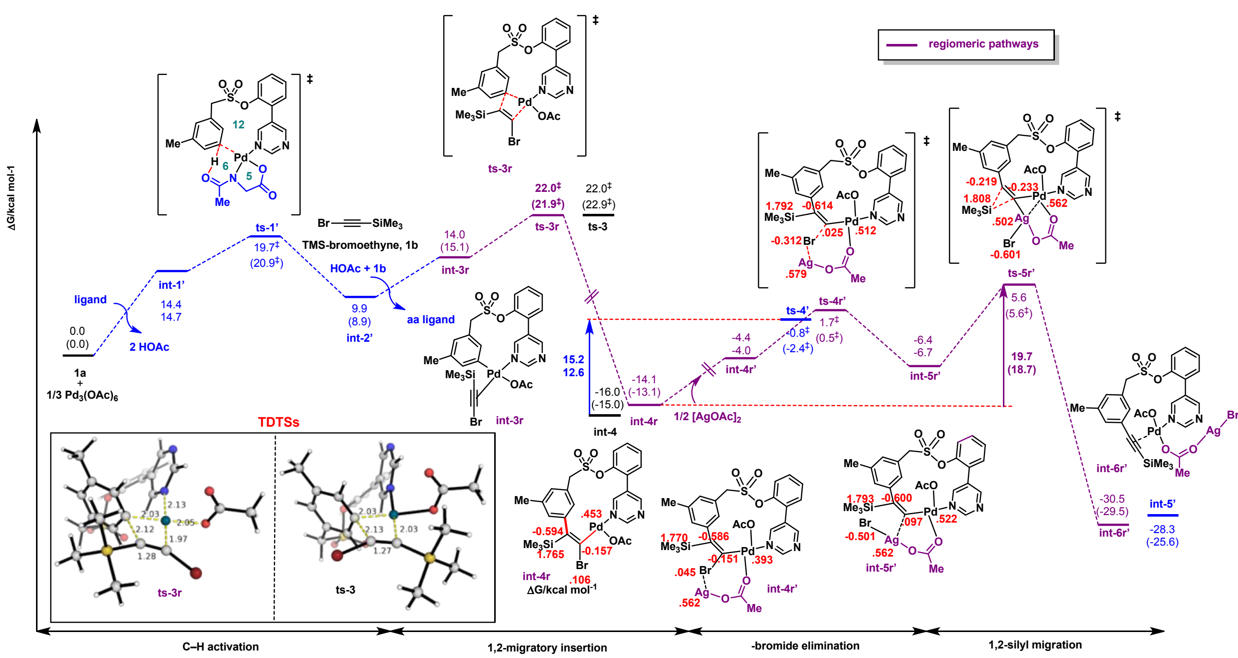

Figure S10. Gibbs energy profile for the regioisomeric insertion of bromoalkyne **1b** and its subsequent β-Br elimination and 1,2-silyl migration to regioconverge on the alkynylated product. Gibbs energies for the key structures from Figure S6 are included for comparison.

Both insertion products are highly exergonic and irreversible. In the latter case, the regioisomeric insertion of **1b** affords a highly stabilized intermediate **int-4r** (at -14.1 kcal mol^{-1}) that further undergoes stepwise loss of bromide (**ts-4r’**) and 1,2-silyl shift (**ts-5r’**) to give regiospecifically the observed alkynylated product. 1,2-silyl shift occurs as the bromide leaves, gaining negative charge (NBO charge (Figure S10, numbers in red) from +0.106 in **int-4r** and +0.045 in **int-4r’** to -0.312 in **ts-4r’** and -0.501 in **int-5r’** and -0.601 in **ts-5r’**), while the carbon atom that it is attached gains carbocationic character (NBO charge at this site that is -0.157 in **int-4r** and -0.151 in **int-4r’** that goes to +0.025 in **ts-4r’** and +0.097 in **int-5r’**. This resembles the anionic 1,n-silyl migration observed in some organocopper-catalysed chemical systems.[34–36]

The rate-limiting step after the insertion product is 1,2-silyl migration **ts-5r’** at 19.7 kcal mol^{-1}, which, although is higher than the barrier of **ts-4’** at 15.2 kcal mol^{-1}, can still occur thermodynamically at the reaction temperature of 80ºC, especially given that the overall TDTS of this regioisomeric pathway is the 1,2-migratory insertion step **ts-3r** at 22.0 kcal mol^{-1}.

ts-3r	**ts-4r’**	**ts-5r’**
22.0‡ (21.9‡)	1.7‡ (0.5‡)	5.6‡ (5.6‡)
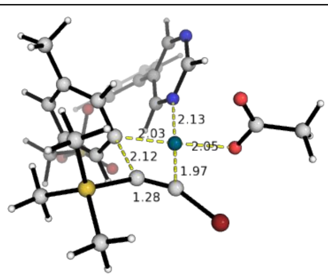	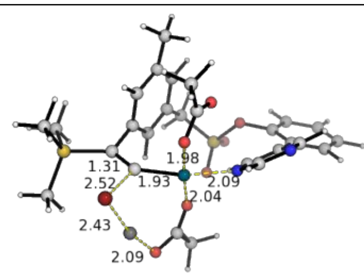	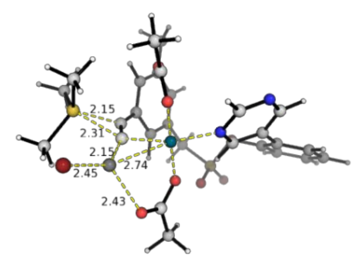
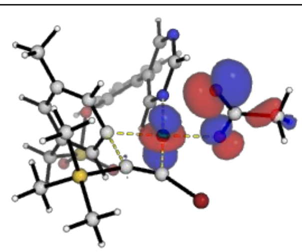	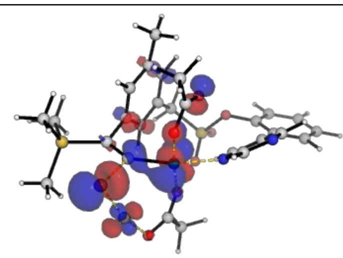	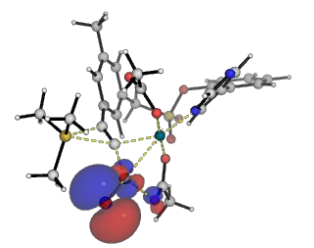

Figure S11. Optimised structures and HOMOs for TSs in Figure S10.

2.6.9 C–H activation site selectivity studies

The site-selectivity of arene activation was then investigated. The *ortho-*/*para*-positions on the arene for potential activation were compared to *meta*-activation (Table S11). The C–H activation and the 1,2-migratory insertion steps were studied. 1,2-migratory insertion was the TDTS for *meta*- and *para*-activation, whereas C–H activation was the TDTS for *ortho*-activation. Application of simple transition state theory (TST) suggests that the *para*-alkynylated product would be disfavoured by 1 in 41, and that the *ortho*-alkynylated product 1 in ~8000.

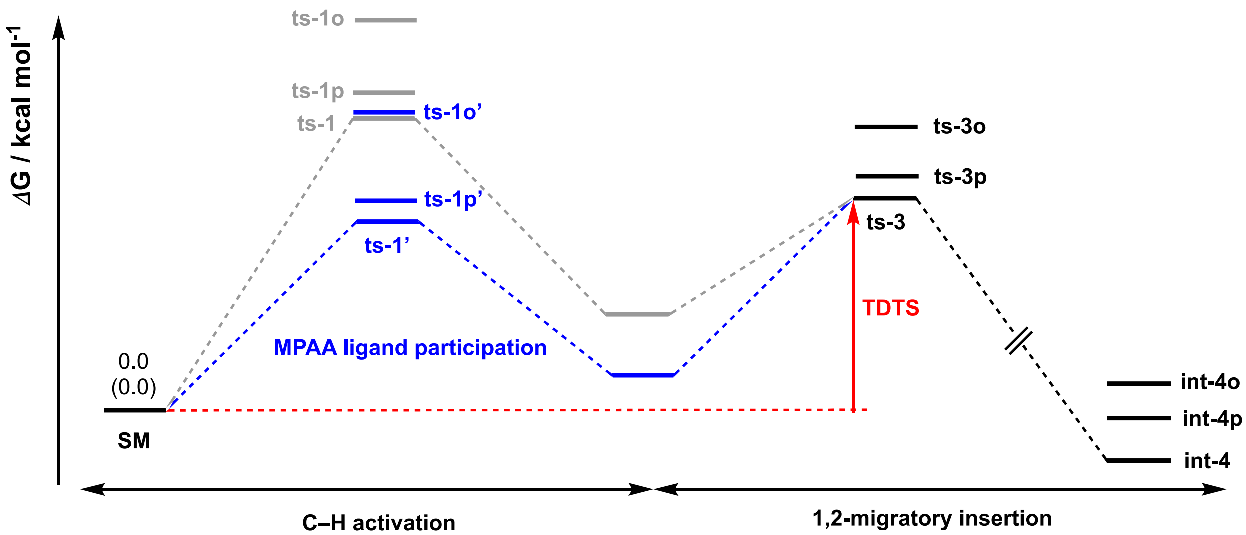

C–H activation site	ts-1x	ts-1x'	ts-3x	int-4x	Overall barrier
meta- (x=nil)	28.0‡ (29.5‡)	19.7‡ (20.9‡)	**22.0‡ (22.9‡)**	-16.0 (-15.0)	**22.0‡ (22.9‡)**
para- (x=p)	29.4‡ (29.4‡)	22.2‡ (21.6‡)	**24.6‡ (23.3‡)**	-9.9 (-10.1)	**24.6‡ (23.3‡)**
ortho- (x=o)	36.2‡ (35.2‡)	**28.3‡ (28.8‡)**	26.8‡ (26.1‡)	-4.5 (-4.4)	**28.3‡ (28.8‡)**

Table S11. Site selectivity study for alkynylation. The highest activation barriers (TDTS) were given in bold.

The optimised structures, HOMOs and non-covalent interaction (NCI) plots for 1,2-migratory insertion are given in Figure S12. We observed that the NCIs are rather similar in all 3 TSs. In earlier studies of a similar system,[10] the ring strain in *ortho*-selective TS is much higher than either *meta*- or *para*-activation. Herein, the *ortho*-selective TS **ts-3o** seemed to undergo a relatively early TS forming C–C bond and thereby relieving the ring strain, as the C–C bond distance is much shorter, at 1.99Å, than either *meta*- or *para*-selective TS, at 2.13Å and 2.15Å, respectively.

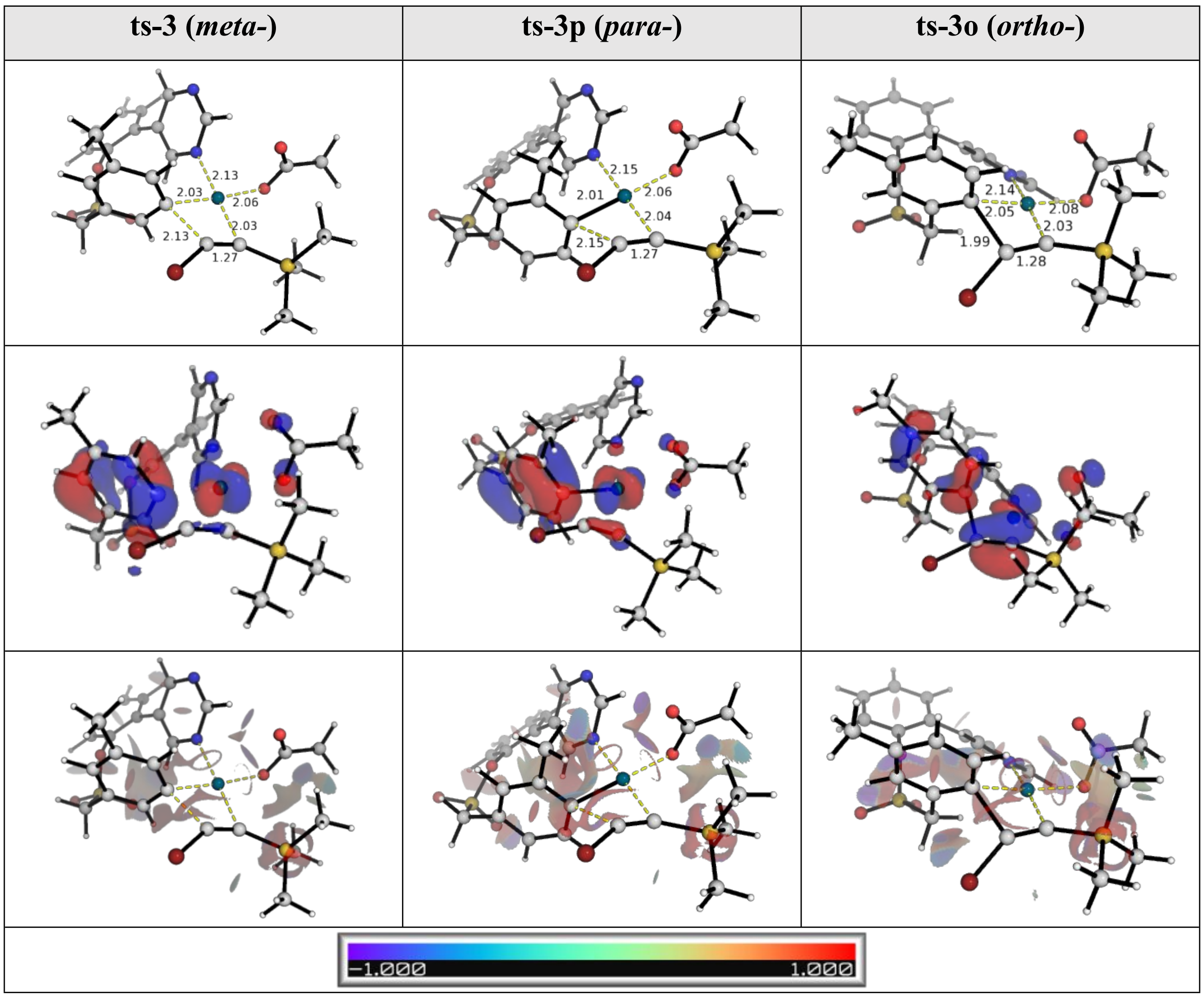

Figure S12. Optimised structures, HOMOs and NCI plots for 1,2-migratory insertion step in arene site-selectivity studies.

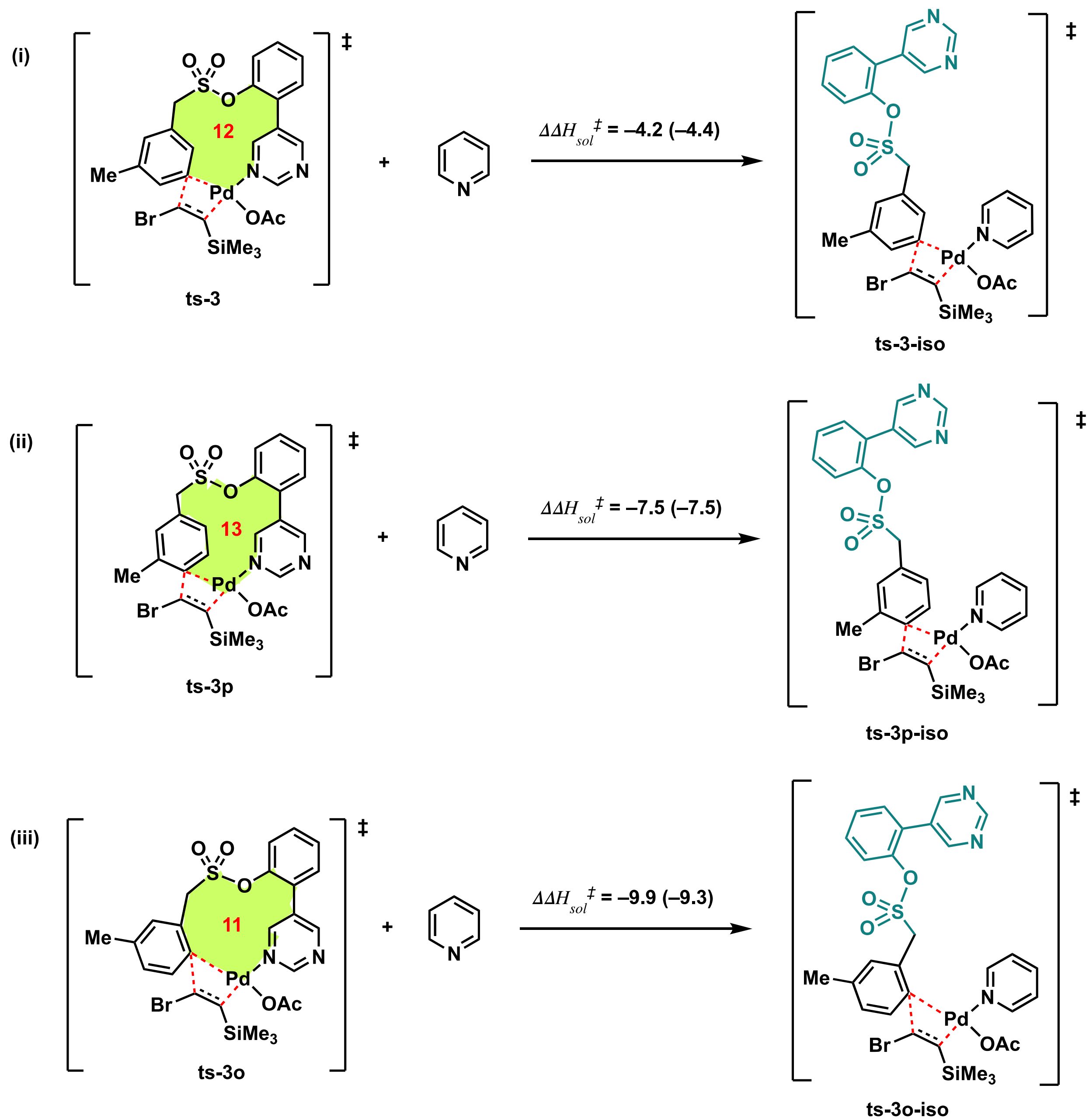

Scheme S4. Computed ring strain involving a hypothetical pyridine ligand for 1,2-migratory insertion step. The enthalpies of the reactions were corrected with SMD solvation model: $\Delta\Delta H^{\ddagger}_{sol} = \Delta H^{\ddagger}_{gas} - \Delta E^{\ddagger}_{gas} + \Delta E^{\ddagger}_{sol}$.

The differences in the ring strain in these 3 TSs were further verified via isodesmic studies,[51,52] (see refs.[19,53] for an example) which confirmed this conclusion (Scheme S4). Specifically, a hypothetical pyridine ligand was used for TS searches to release the ring strain where the directing group (DG) got uncoordinated. Note that in an isodesmic reaction, the total number and type of all bonds in the reactants and the products are preserved. The starting conformation for the DG (in green, Scheme S4) in all 3 cases was made the same in a linear form for subsequent

TS searches. The enthalpies of the reactions were further corrected with SMD solvation model:

$$\Delta\Delta H^{\ddagger}_{\mathrm{sol}} = \Delta\Delta H^{\ddagger}_{\mathrm{gas}} - \Delta\Delta E^{\ddagger}_{\mathrm{gas}} + \Delta\Delta E^{\ddagger}_{\mathrm{sol}}$$

where $\Delta H^{\ddagger}_{gas}$ is the enthalpy change of the reaction in the gas phase at low level of theory for computation, $\Delta E^{\ddagger}_{gas}$ is the energy change of the reaction in the gas phase at low level of theory for computation and $\Delta E^{\ddagger}_{sol}$ is the energy change of the reaction in the solvent phase at high level of theory for computation.

From the enthalpic changes, we can see that there is 4.2 kcal mol^{-1} ring strain in **ts-3** as compared to 7.5 kcal mol^{-1} in **ts-3p** and 9.9 kcal mol^{-1} in **ts-3o**. Their ring strain energy differences are similar to the differences in their activation barriers for this step, as shown in Table S11. The 12-membered *meta*-selective TOF-determining palladacycle (**ts-3**) has the least strain, followed by 13-membered *para*-selective palladacycle (**ts-3p**) and then by 11-membered *ortho*-selective palladacycle (**ts-3o**).

2.6.10 Reaction involving substrate ethynyltrimethylsilane 1c

Experimentally, when the reaction was carried out using ethynyltrimethylsilane **1c** instead of **1b**, the reaction did not occur; the substrate was recovered. Detailed TS searches showed that silver could not participate in the beta-H elimination step, perhaps unsurprising since silver cation cannot interact with a leaving hydride. The full Gibbs energy profile in Figure S13 suggests that, as a result, beta-H elimination giving a Pd–H (**ts-4H**, Figure S14) and the subsequent reductive elimination of acetic acid to generate Pd(0) (**ts-5H**, Figure S14, overall barrier of 30.5 kcal mol^{-1}) are high in energy barrier, thus being kinetically unfavourable. In fact, the TDI for the reaction is **int-4H**, making the overall barrier for subsequent catalytic cycles to be > 50.0 kcal mol^{-1}, thus not thermally accessible at the reaction temperature.

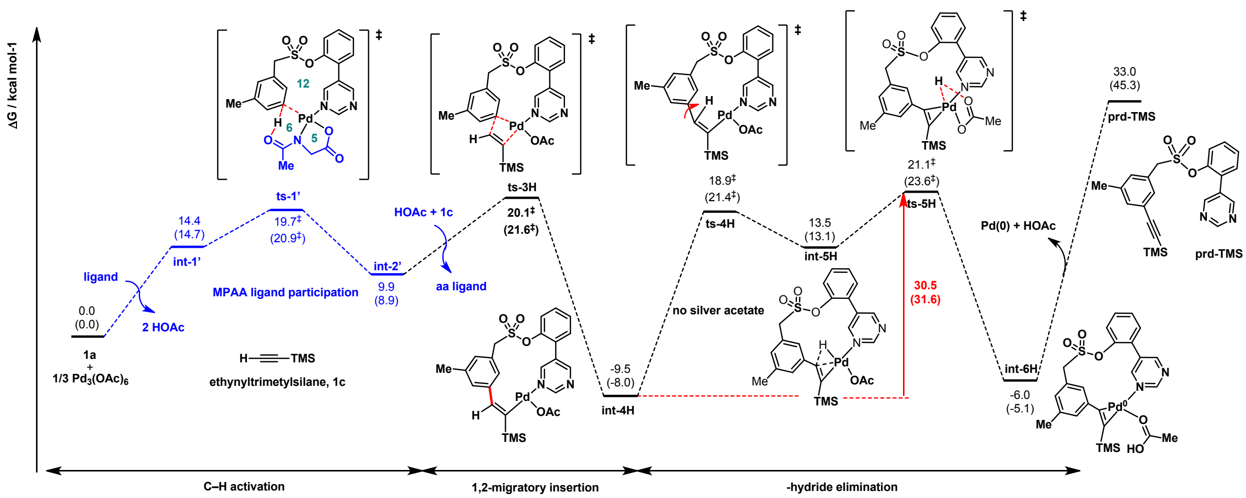

Figure S13. Gibbs energy profile for the reaction involving ethynyltrimethylsilane **1c**.

In addition, the overall reaction gives endergonic intermediates relative to the 1,2-migratory insertion intermediate **int-4H**, making this reaction thermodynamically unfavourable. The potentially poor orbital overlap between the σ_{CH} of the beta-hydride and the d-orbital of Pd in **ts-4H** and that between lone pair orbital of acetate and $\sigma^*_{Pd\text{–}H}$ of the metal-hydride in **ts-5H** could be the reason for this unfavourability; the ring strains in the palladacycle (distorted geometries) potentially contribute to the high activation barriers too (Figure S14). In addition, the release of product **prd-TMS** from the end Pd(0) species is highly unfavourable thermodynamically. Therefore, both steric and electronic factors disfavour the reaction of substrate **1c** in this alkynylation reaction. Experimentally, it is also possible that homocoupling of terminal alkynes occurs due to the presence of copper additives,[54–59] rendering this substrate incompetent.

ts-3H	ts-4H	ts-5H
20.1‡ (21.6‡)	18.9‡ (21.4‡)	21.1‡ (23.6‡)
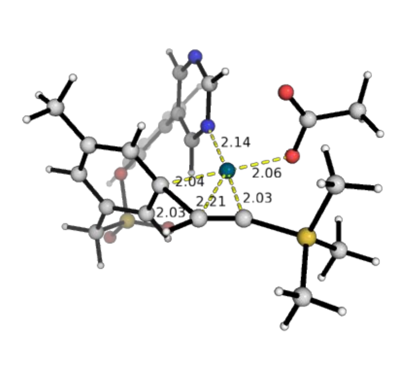	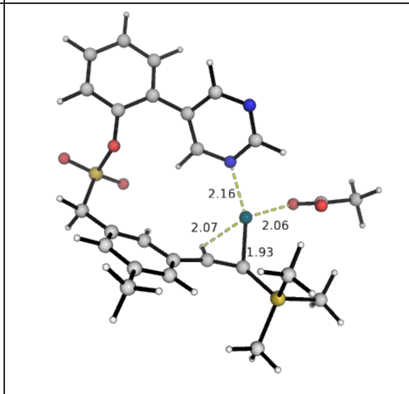	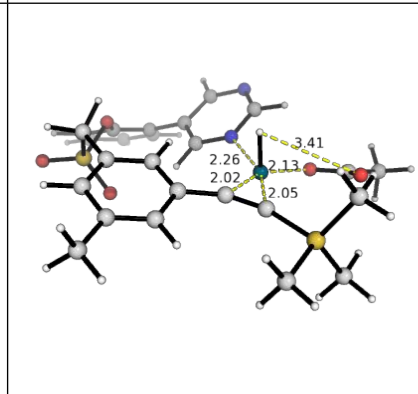
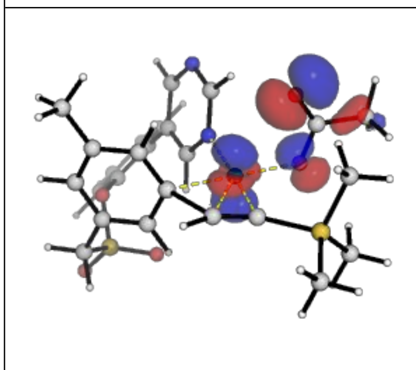	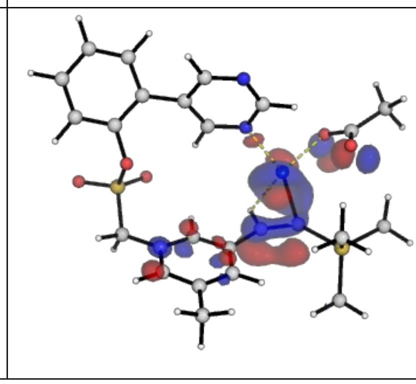	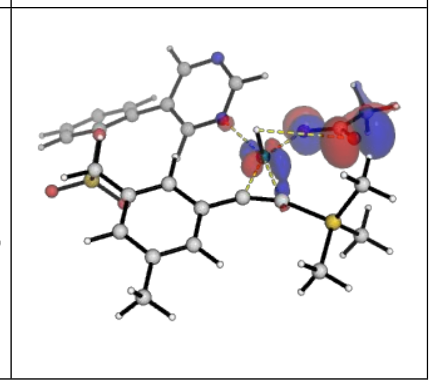

Figure S14. Optimised structures and HOMOs for TSs in Figure S12.

2.6.11 Reactivity for substrate bromoethynylbenzene 1d

When bromoethynylbenzene **1d** was used experimentally, the reaction has a poor yield; the majority of the substrate was recovered unreacted. The full Gibbs energy profiles for the reaction using substrate bromoethynylbenzene **1d** are shown in Figure S15. These energy profiles indicate that the irreversible 1,2-migratory insertion steps occurred unselectively (**ts-3P** and **ts-3rP** have the same activation barrier, at 24.5 kcal mol^{-1}), where either carbon of the acetylene functional group of the substrate can form C–C bond with the activated arene. This is similar to the reaction using silylated alkynylbromide **1b** (**ts-3** and **ts-3r**, Figure S10). However, for the regioisomeric insertion, the subsequent 1,2-phenyl shift (**ts-5r'P**, at 28.3 kcal mol^{-1}) for one of the regioisomeric paths had a much higher barrier than 1,2-silyl shift (**ts-5r'**, Figures S10 and S11) using substrate **1b**. The 1,2-silyl migration on carbon atoms can occur much more readily than 1,2-aryl migration on carbon atoms. Similar 1,2-silyl migration reactions have been previously reported.[60,61]

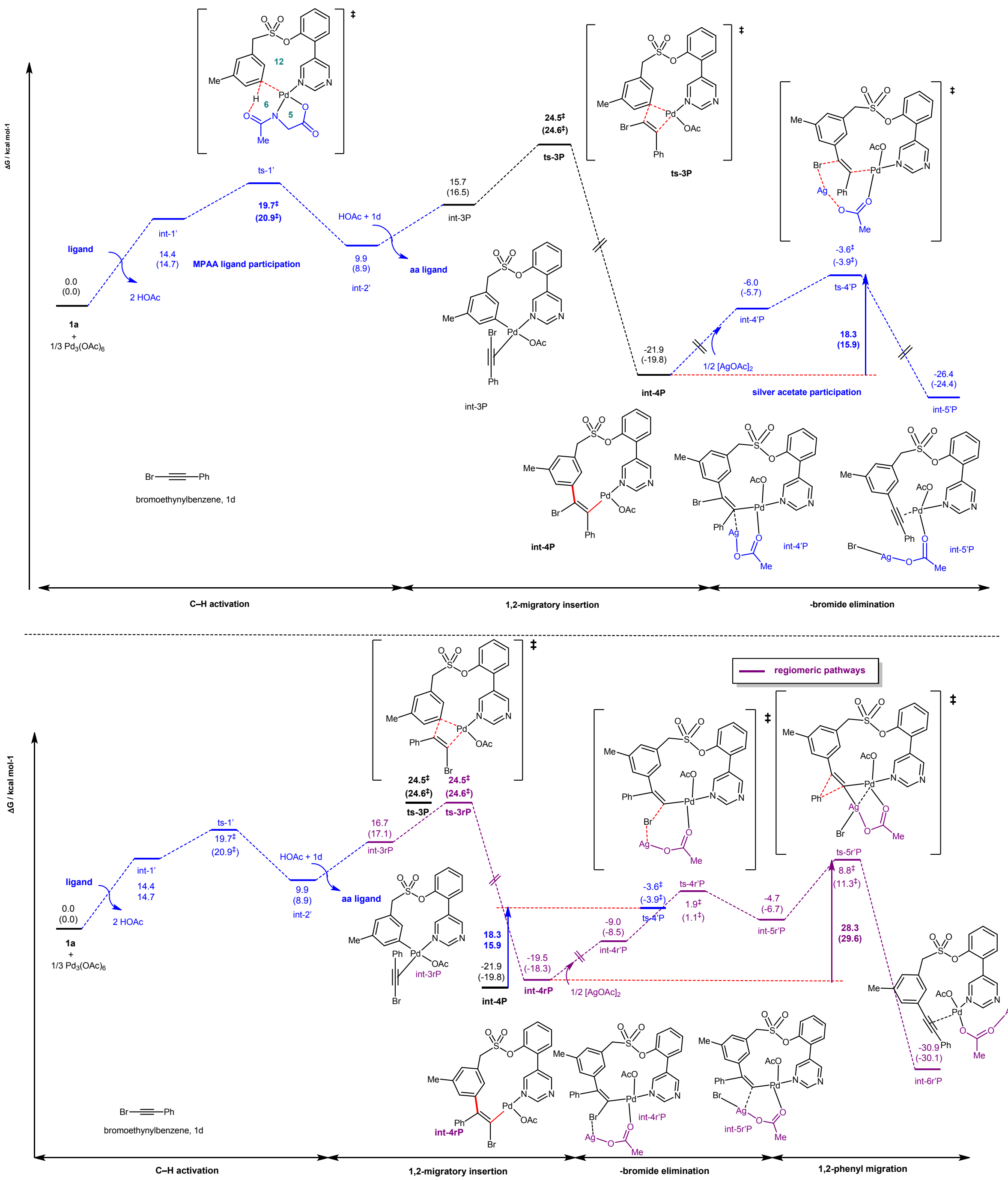

Figure S15. Gibbs energy profiles (two regioisomeri pathways) for the reaction involving bromoethynylbenzene **1d**.

Nevertheless, computations seem to suggest that the reaction is at least kinetically and thermodynamically feasible as that using substrate **1b**, though the selectivity/ regioconvergency of the product formation might not be as good (barrier of 28.3 kcal mol^{-1}, Figure S15) as using substrate **1b** (barrier of 19.7 kcal mol^{-1}, Figure S10), perhaps unsurprising as the phenyl group has a higher difficulty than the trialkylsilyl group in carrying out 1,2-migration.

The reactivity could potentially be hindered due to the propensity of bromoethynyl-benzene **1d** to form favourable π-π stacking[62–64] within themselves and with arene starting material; it can also form cation-π interactions[64,65] with Pd(II), making them less available for reaction. This is possible as the relative comparison of $[Pd(substrate)_2]^{2+}$ complexes showed that Pd(II) coordination with two bromoethynylbenzene **1d** molecules $[Pd(\mathbf{1d})_2]^{2+}$ is 11.9 (15.3) kcal mol^{-1} more stabilised than with two bromoethynyl-trimethylsilane **1b** molecules $[Pd(\mathbf{1b})_2]^{2+}$ (Figure S16).

$$Pd^{2+} + 2\,x \xrightarrow{\Delta G_r} [Pd(x)_2]^{2+} \;;\quad x = 1b, 1d$$

Pd-1d2-c1	Pd-1d2-c2	Pd-1b2-c1	Pd-1b2-c2
-188.7 (-203.8)	-179.0 (-198.6)	-176.8 (-186.8)	-171.1 (-184.9)
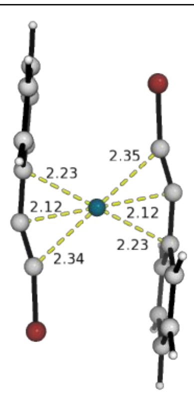	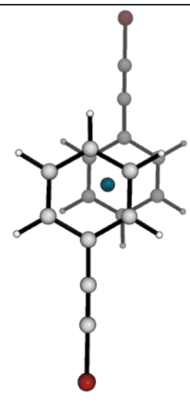	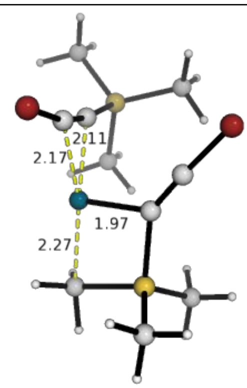	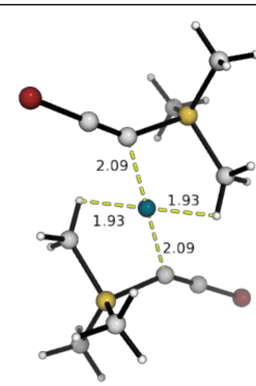

Figure S16. Gibbs energy of reaction (*ΔG*r, in kcal mol^{-1}) for the coordination complexes of substrates **1b** and **1d** with Pd(II) cation.

2.6.12 Possible role of copper according to computational studies

Experimentally, it was shown that the yield of the reaction is augmented by the addition of copper(II) acetate salt. The role of this copper additive was explored computationally. The most stable form of $Cu(OAc)_2$ is in triplet spin state (Figure S17 (a)), thus, we take ½ of triplet copper(II) acetate dimer as the reference species. Normally, any copper additive is assumed to play a role as a co-oxidant to regenerate the main catalyst or as a source of acetate ions; computational studies of these reactions do not normally consider its explicit role in the catalytic cycle and its exact roles in the catalytic cycle are poorly understood.[66–68] The explicit role of $Cu(OAc)_2$ salt was demonstrated in one study by Funes-Ardoiz and Maseras, who show that copper additive can act as a cooperative catalyst in the reductive coupling of a C–O bond in isocoumarin formation through a Rh–Cu heterobimetallic TS.[69] We wonder if $Cu(OAc)_2$ plays a similar role as AgOAc in the present reaction in forming a heterometallic complex in the β-bromide elimination step, potentially forming $CuBr_2$ as a side product.

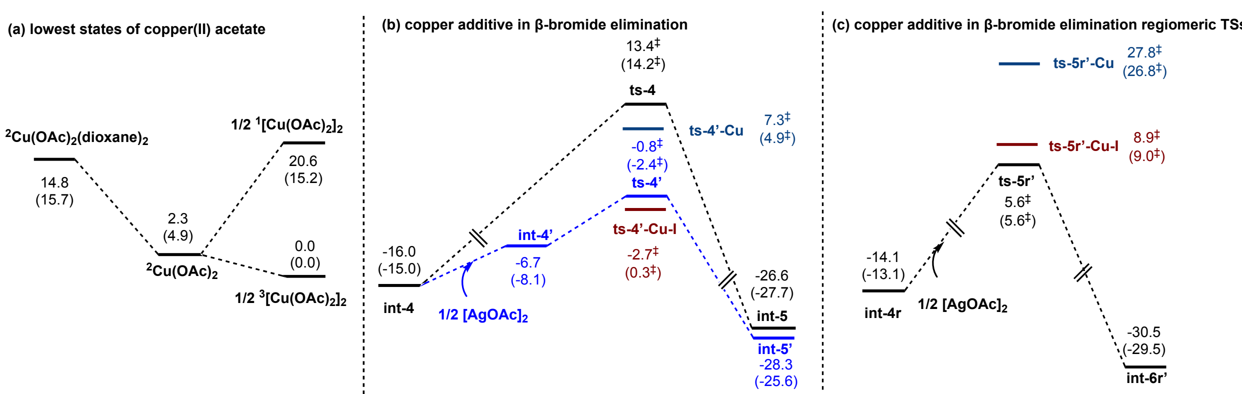

Figure S17. (a) Stability of mononuclear and dinuclear (singlet vs triplet) copper(II) acetate species. (b) TSs with copper additive in β-bromide elimination step, and (c) TSs with copper additive in β-bromide elimination step for the regiomeric reaction.

We found that the Pd–Cu(II) heterobimetallic TS (**ts-4'-Cu**, 7.3 kcal mol^{-1}, Figure S18) gives an overall barrier of 23.3 kcal mol^{-1}; this is 8.1 kcal mol^{-1} higher than the Pd–Ag heterobimetallic TS (**ts-4'**, -0.8 kcal mol^{-1}), although it is 6.1 kcal mol^{-1} lower in activation barrier than the β-bromide elimination TS without any metal additive (**ts-4**, 13.4 kcal mol^{-1}) (Figure S17 (b)). The Pd–Cu(II) heterobimetallic TS for the regiomeric rate-determining 1,2-silyl group migration (**ts-5r'-Cu**, 27.9 kcal mol^{-1}, Figure S18) also has a higher barrier than the Pd–Ag heterobimetallic TSs (**ts-5r'**, 5.6 kcal mol^{-1}) (Figure S17 (c)).

Pd–Cu(II) heterobimetallic TSs	
ts-4'-Cu	**ts-5r'-Cu**
7.3‡ (4.9‡)	27.9‡ (26.8‡)
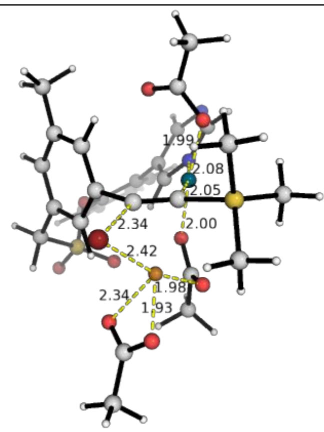	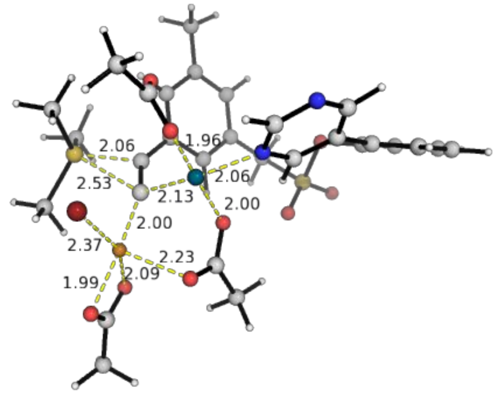
Pd–Cu(I) heterobimetallic TSs	
ts-4'-Cu-I	**ts-5r'-Cu-I**
-2.7‡ (0.3‡)	8.9‡ (9.0‡)
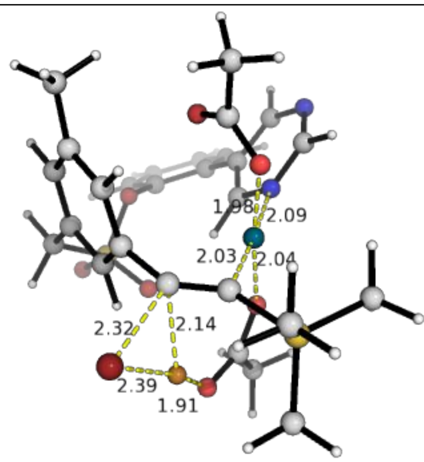	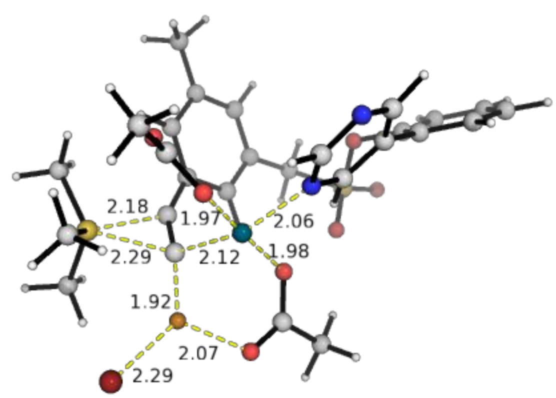

Figure S18. Optimised structures for Pd–Cu(II) and Pd–Cu(I) heterobimetallic TSs using $Cu(OAc)_2$ and CuOAc additive respectively.

As the Cu(II) additive also acts as an oxidant, we considered if the reduced form Cu(I) had any effect on the activation barriers for the β-bromide elimination step. We found that the use of CuOAc gives a Pd–Cu(I) heterobimetallic TS for the β-bromide elimination step (**ts-4'-Cu-I**, -2.7 kcal mol^{-1}, Figure S17) with a lower activation barrier than the use of AgOAc (**ts-4'**, -0.8 kcal mol^{-1}). For the regiomeric pathway, the use of AgOAc has lower activation barrier (**ts-5r'**, 5.6 kcal mol^{-1}, Figure S10) than CuOAc (**ts-5r'-Cu-I**, 8.9 kcal mol^{-1}). Cu(I) additive give lower barriers than Cu(II) additive for both heterobimetallic TSs.

We wondered if $Cu(OAc)_2$ helps to regenerate the silver salt. This is unlikely as 2 equivalents each of $Cu(OAc)_2$ and AgOAc were used in the reaction. We calculated the thermodynamics of the following reaction:

$$\mathbf{{}^{1}[AgBr]_2 + 1/2\ {}^{3}[Cu(OAc)_2]_2 \longrightarrow {}^{1}[AgOAc]_2 + 1/2\ {}^{3}[CuBr_2]_2}$$

and found that this reaction has an uphill Gibbs energy of reaction of 16.4 (17.1) kcal mol^{-1}, thus ruling out this possibility.

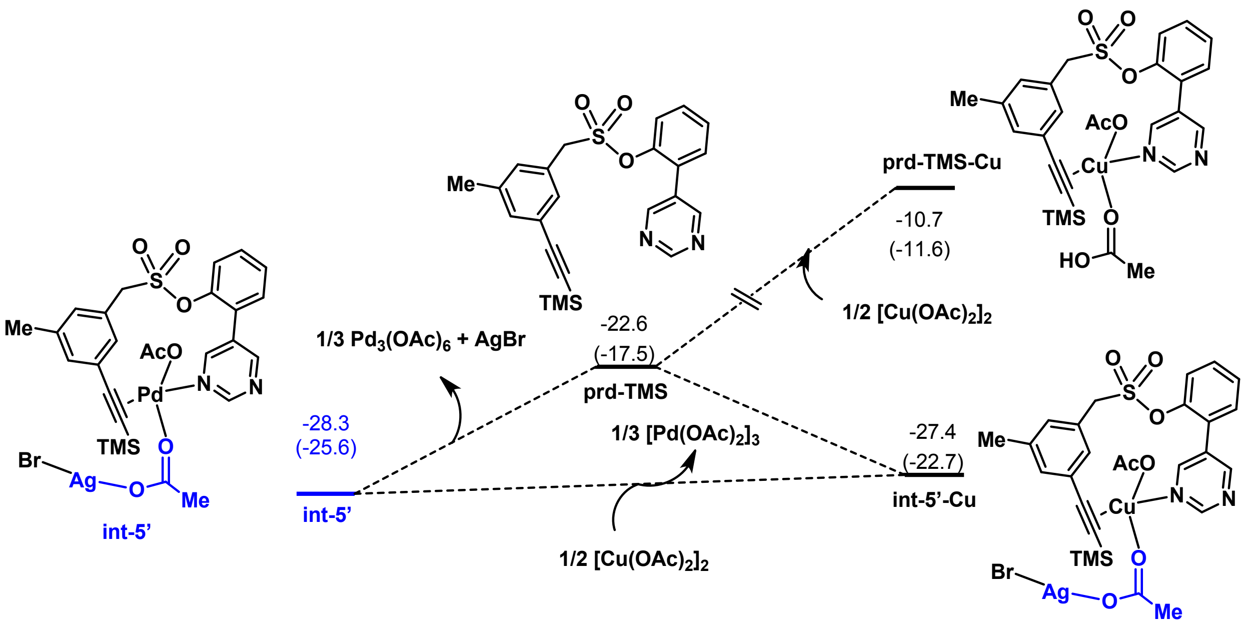

Figure S19. Transmetallation in the product release to free up palladium catalyst.

Next, we checked if the copper salt helps in the release of palladium catalyst from its coordination to the alkynylated product, so that it can undergo the next catalytic cycle. Coordination of ½ $[Cu(OAc)_2]_2$ to the product releases the palladium catalyst for the next cycle. This transmetallation is more thermodynamically favourable than the direct release of product from **int-5'** (Figure S19), suggesting that it could possibly increase the yield by making palladium catalyst more available after each catalytic cycle.

2.6.13 Comparative study of other trialkylsilyl and siloxy-substituted substrates

We compared the chemical reactivity and selectivity of the other substrates used in the present transformation, namely that of (bromoethynyl)triisopropylsilane, or hereafter TIPS-bromoalkyne **1e**; (bromoethynyl)tri*tert*-butyldimethylsilane or TBDMS-bromoalkyne **1f**; (bromoethynyl)triethylsilane or TES-bromoalkyne **1g**; and siloxy-substituted substrate ((1-(bromoethynyl)cyclohexyl)oxy)trimethylsilane **1h**. The optimised structures are named as per TMS-bromoalkyne, except where the the substrate name is added to the front of the structures, for example, **1e-ts-3** gives the "normal" 1,2-migratory insertion TS for substrate **1e**.

The energy profile for TIPS-bromoalkyne 1e is shown in Figure S20. As we can see, the regioselectivity can be controlled in this case, where the bulky TIPS-group favours the "normal" 1,2-migratory insertion **1e-ts-3** over the other one **1e-ts-3r** by 1.9 kcal mol^{-1}. This is likely due to the unfavourable steric clashes between the triisopropylsilyl group and the arene in the regioisomeric 1,2-migratory insertion TS **1e-ts-3r**, as shown by the NCI plots in Figure S21. This finding is in accordance with the steric control of regioselective of migratory insertion of C–H alkynylation observed by Sarpong, Musaev, and co-workers.[56]

NBO second-order perturbation theory calculations were used to study the potential for a β-Pd effect as observed by Musaev and Sarpong, whereby a filled σ(Pd–C) donates electron density to the σ*(C–Br) orbital. Although we do not observe such an interaction in the carbopalladation TS, it was apparent in the resulting intermediate: in int4 the computed delocalization energy from the σ(Pd-C) to σ*(C-Br) is 22.5 kcal/mol. In contrast, in int4r we found a σ(Pd-C) to σ*(C-Si) delocalization of 6.9 kcal/mol, along with a σ(C-C) to σ*(C-Br) delocalization of 11.0 kcal/mol. These results are consistent with hyperconjugation playing a role in stabilizing int4 over int4r.

It was further found that the 1,2-silyl migratory following regioisomeric insertion TS **1e-ts-3r** has a low activation barrier of 19.6 kcal mol^{-1}, which is much lower than the barrier for the turnover-limiting 1,2-insertion step, indicating that the regioconvergency of product will still be achieved regardless of the regioselectivity step. The proposed 1,2-silyl migration in **1e-ts-5r'** is the same as for the TMS-alkynylbromide case as discussed in the main manuscript. As before, following the 1,2-migratory insertion step, the AgOAc ligand-assisted heterobimetallic β-bromide elimination TS **1e-ts-4'** has a lower activation barrier (15.2 kcal mol^{-1}) than the TDTS **1e-ts-3** with a barrier of 23.6 kcal mol^{-1}. The final alkynylated product is once again energetically very downhill and thermodynamically favourable.

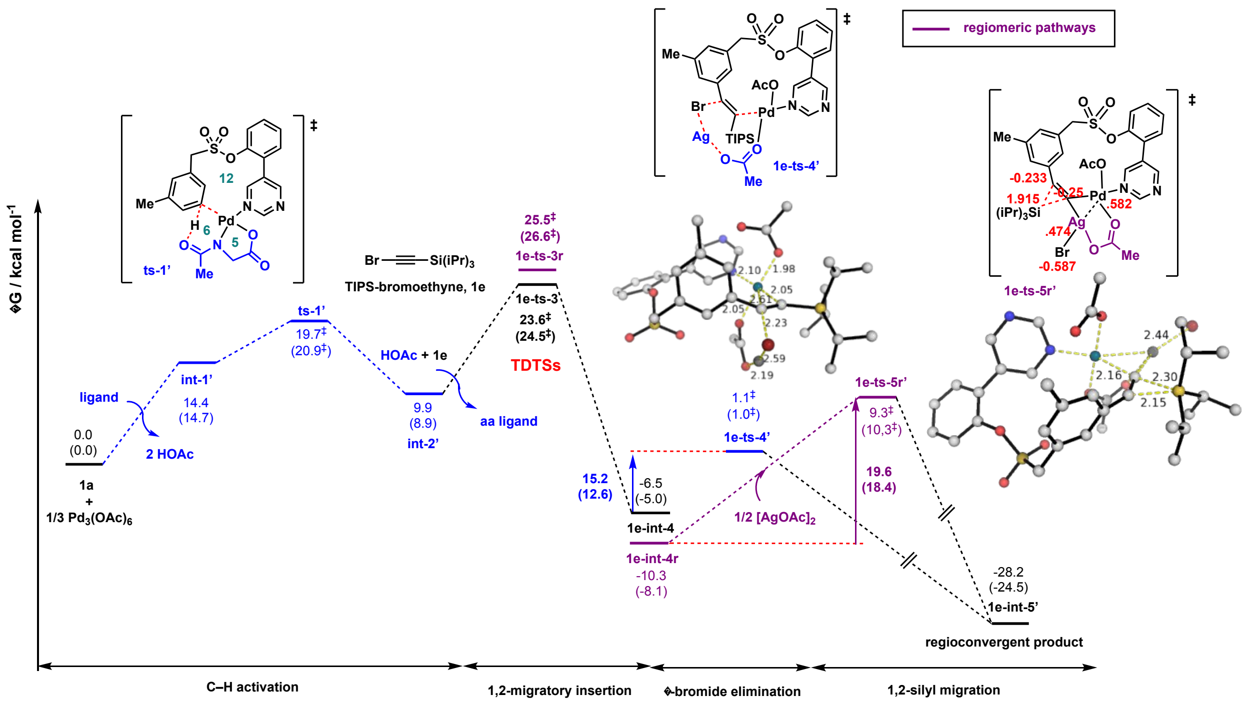

Figure S20. Gibbs energy profile for the present transformation using substrate TIPS-alkynylbromide **1e**.

1e-ts-3	1e-ts-3r
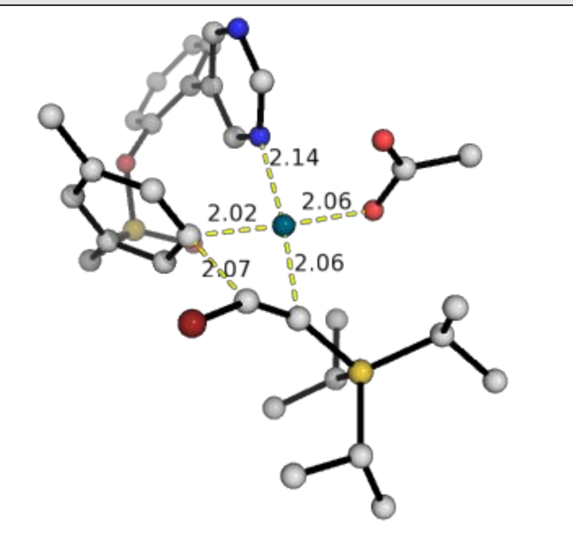	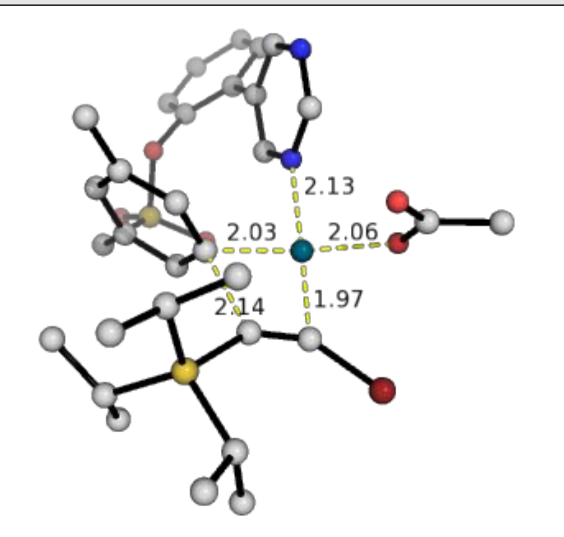

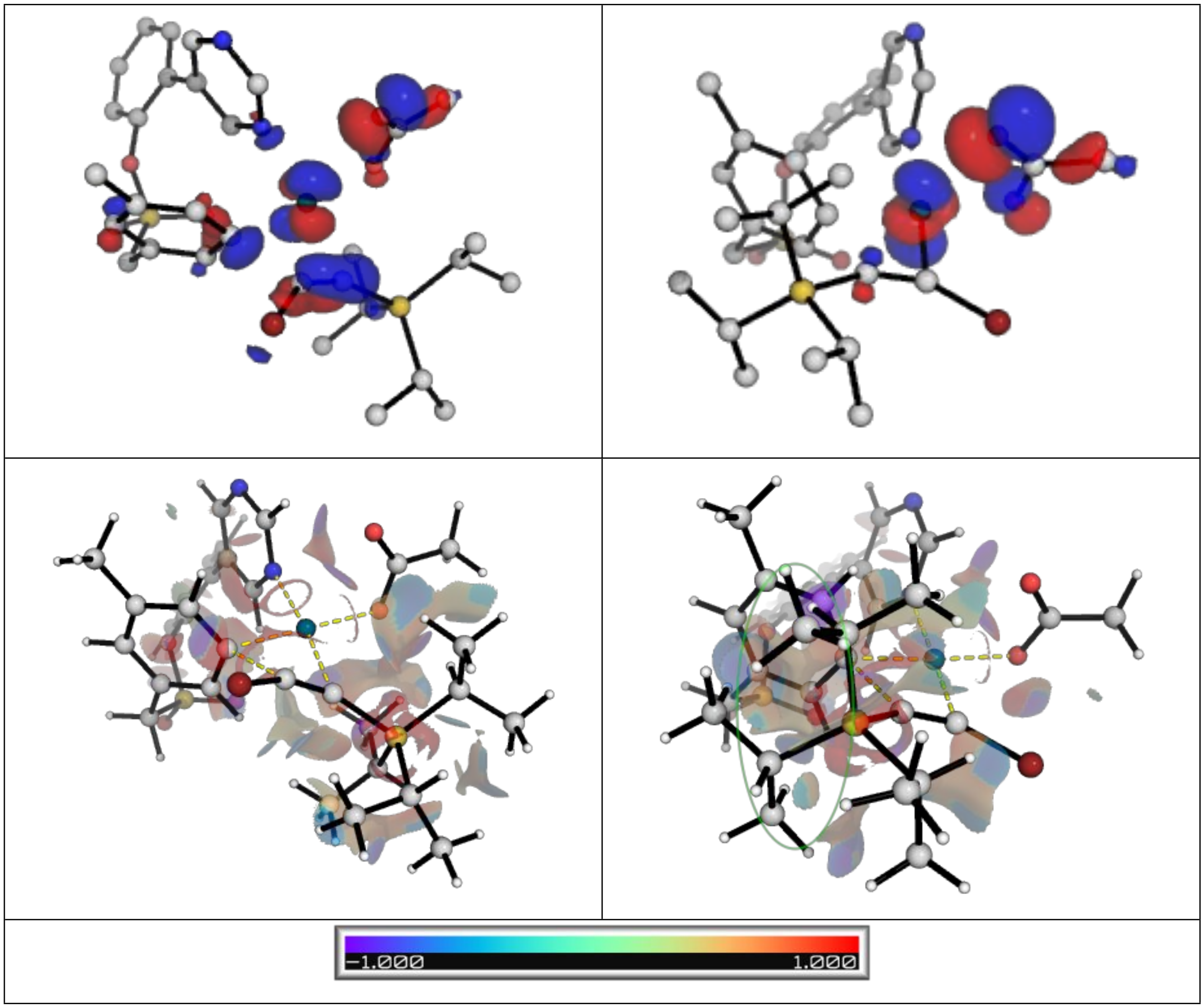

Figure S21. Optimised structures, HOMOs and NCI plots for the regioisomeric 1,2-migratory insertion steps for substrate TIPS-alkynylbromide **1e.**

The reaction using the other trialkylsilylbromoalkyne substrates TBDMS-bromoalkyne **1f** and TES-bromoalkyne **1g** are similarly considered; the results are shown in Figures S22 to S25. We can see that for all trialkylsilylbromoalkynes, the 1,2-migratory insertion is the TDTS. The regioselectivity is in favour of one over the other due to possible larger steric constraints in one of the TS (**ts-3r**) than the other (**ts-3**). We can see that **1f-ts-3** is favoured by 1.1 kcal mol^{-1} than the regioisomeric pathway **1f-ts-3r** (Figure S22) and that **1g-ts-3** is favoured by 2.2 kcal mol^{-1} than the regioisomeric pathway **1g-ts-3r** (Figure S24). However, in all these cases, the 1,2-silyl migration following one of the regioisoermic pathways has lower activation barrier than the TDTS, indicating that the regioconvergency of product will be observed regardless of the regioselectivity at the turnover-limiting insertion step.

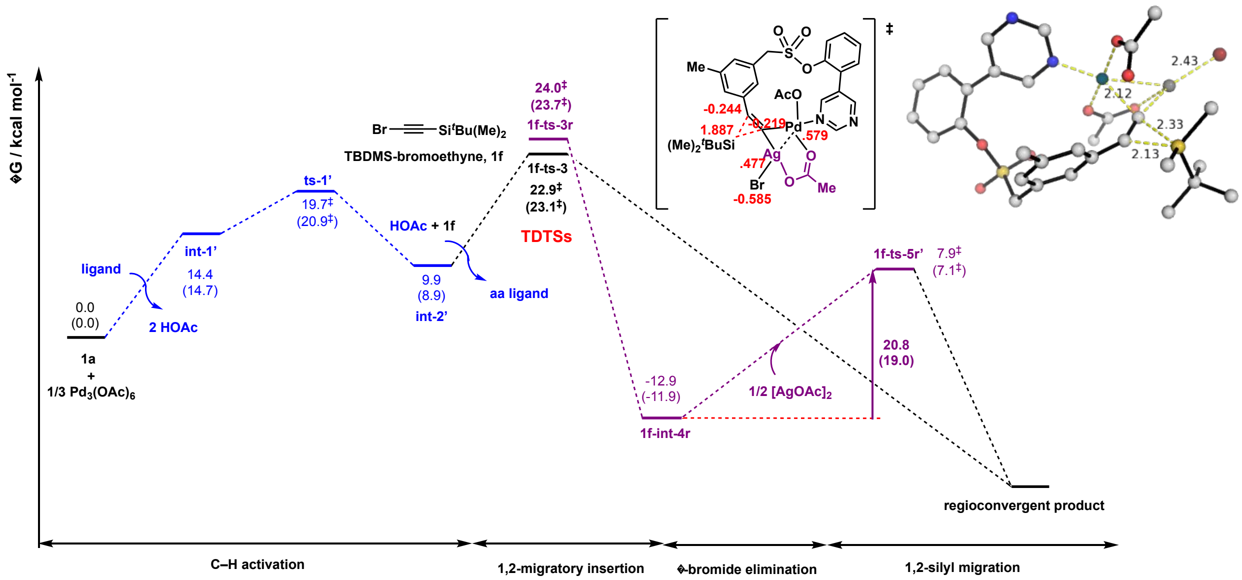

Figure S22. Gibbs energy profile for the present transformation using substrate TBDMS-alkynylbromide **1f**.

1f-ts-3	1f-ts-3r
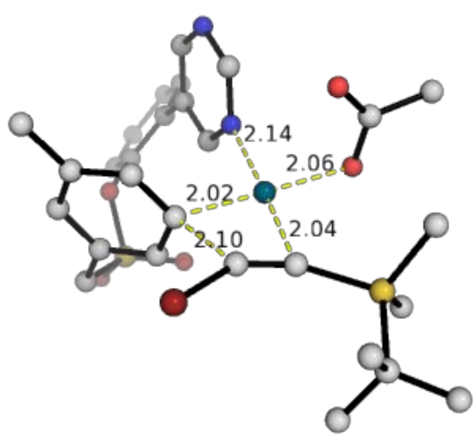	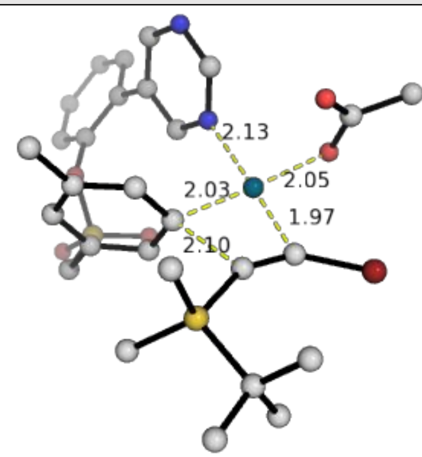

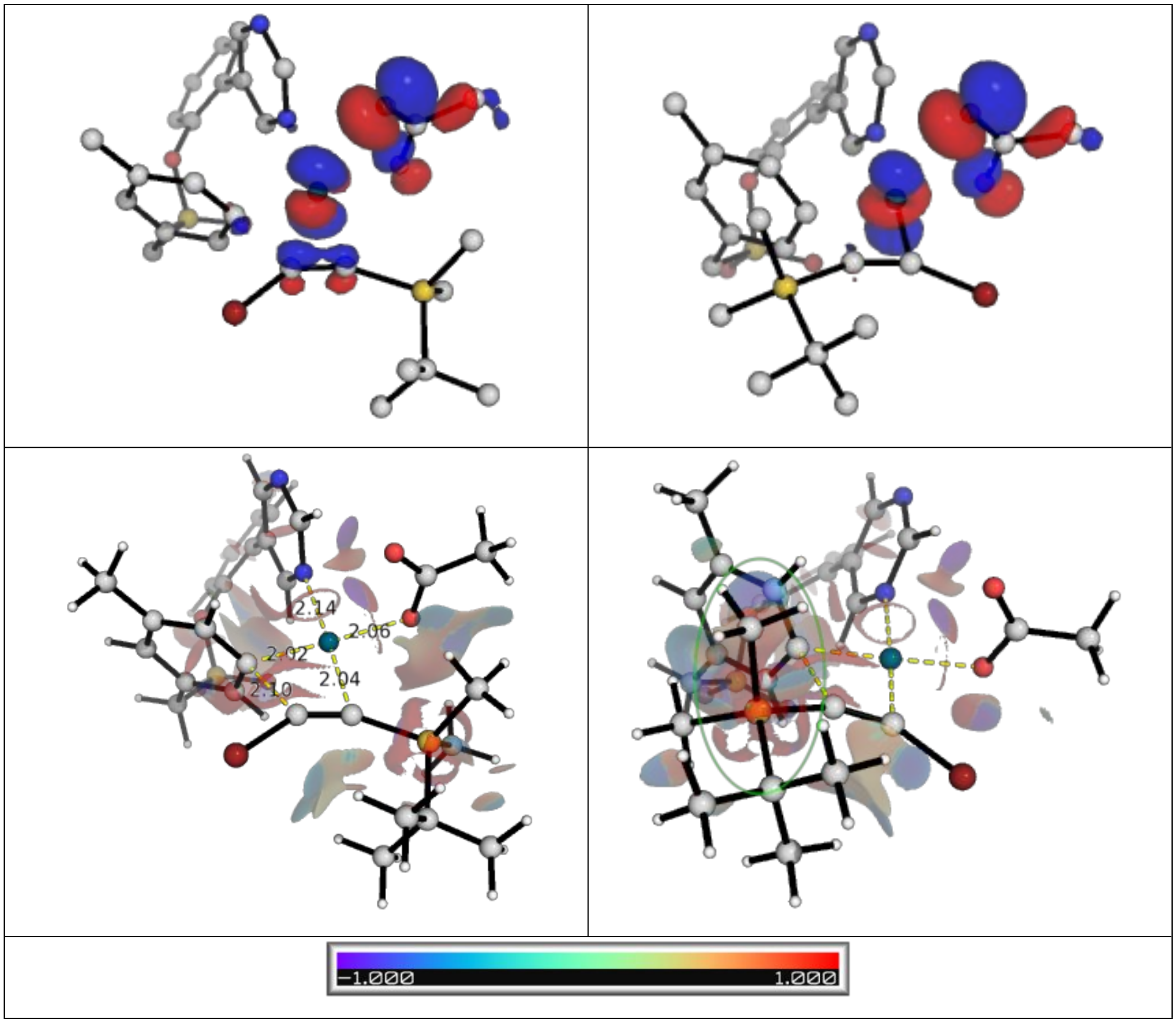

Figure S23. Optimised structures, HOMOs and NCI plots for the regioisomeric 1,2-migratory insertion steps for substrate TBDMS-alkynylbromide **1f.**

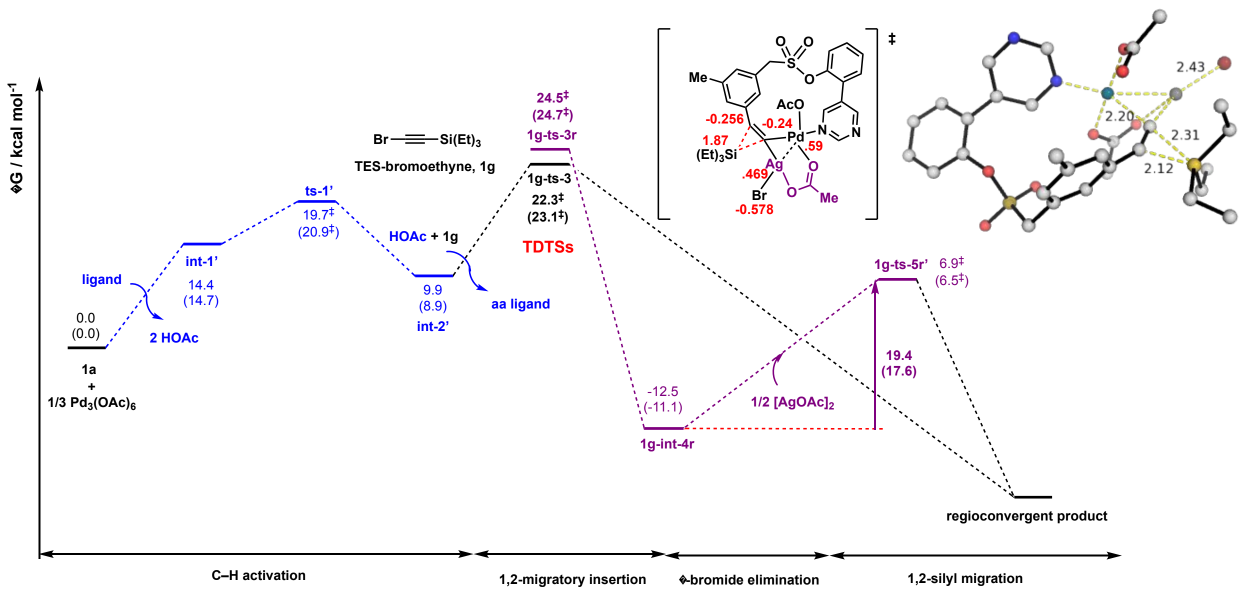

Figure S24. Gibbs energy profile for the present transformation using substrate TES-alkynylbromide **1g**.

1g-ts-3	1g-ts-3r
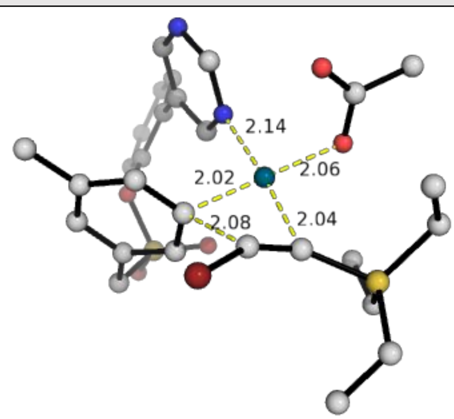	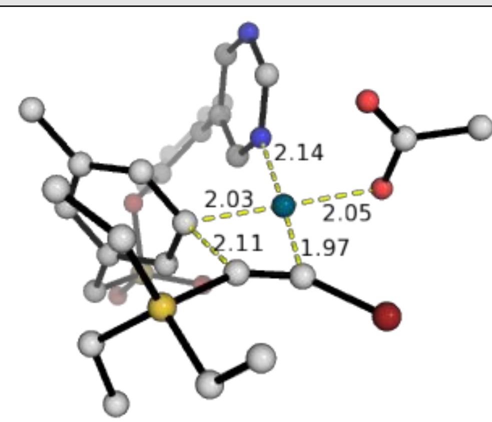

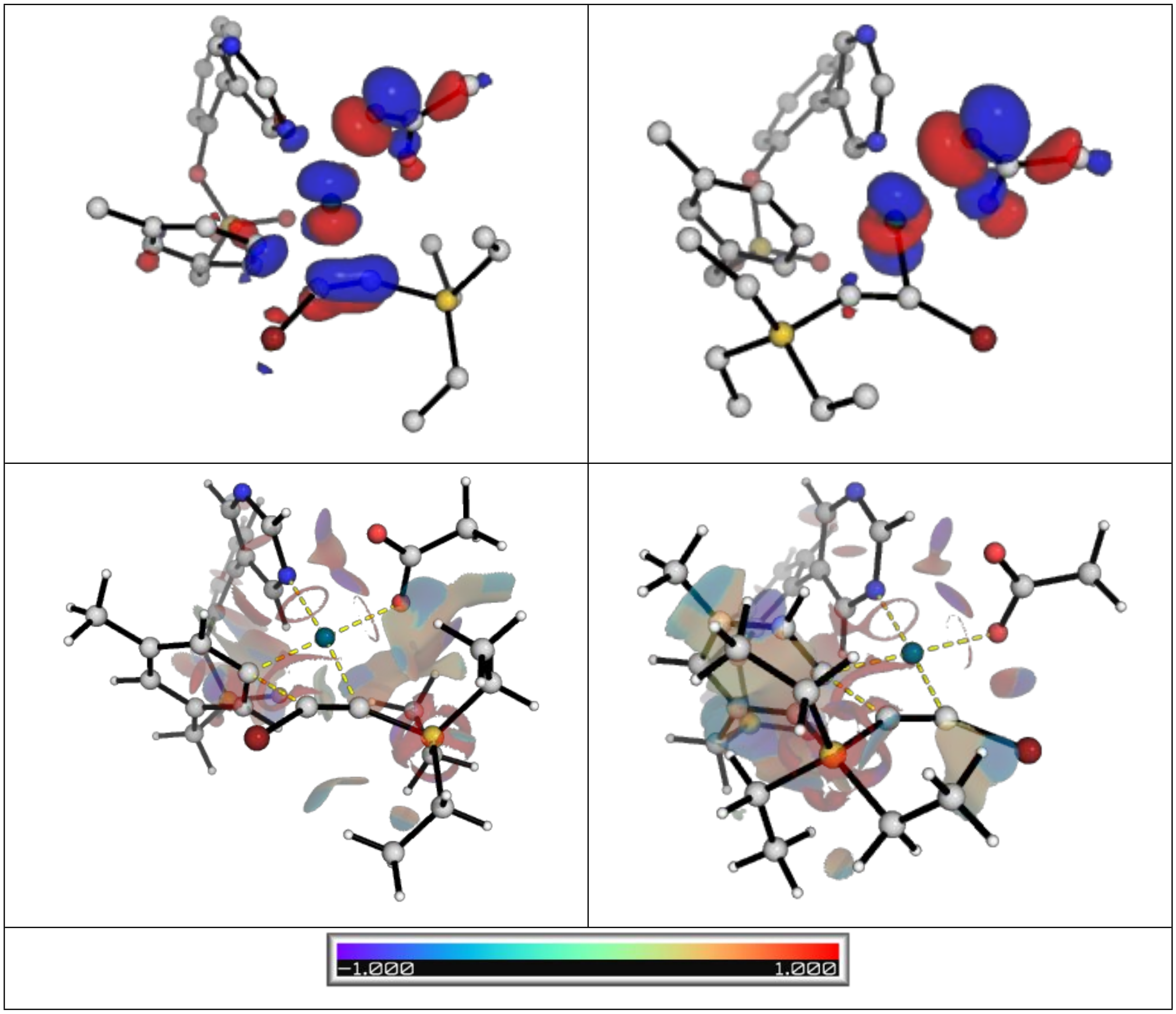

Figure S25. Optimised structures, HOMOs and NCI plots for the regioisomeric 1,2-migratory insertion steps for substrate TES-alkynylbromide **1g.**

For the siloxy-substituted substrate ((1-(bromoethynyl)cyclohexyl)oxy)trimethylsilane **1h**, we compared the TDTS 1,2-migratory insertion step for regioselectivity. The results are given in Figure S26. We can see that the TS for the "correct" regioselectivity is favoured by slightly better sterics (as evidenced by the NCI plots) as the bulky siloxy group is kept away from the C–C bond formation centre. This is in agreement with the steric control of regioselectiviy observed in similar reactions reported by Sarpong, Musaev, and co-workers,[56] as noted previously.

1h-ts-3	**1h-ts-3r**
ΔG‡ = 25.5‡ (26.5‡)	26.7‡ (27.8‡)
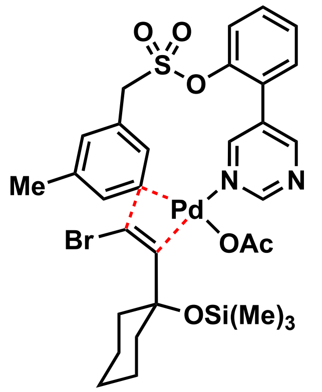	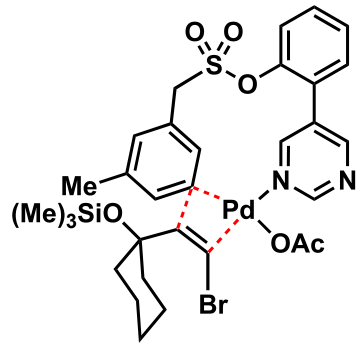
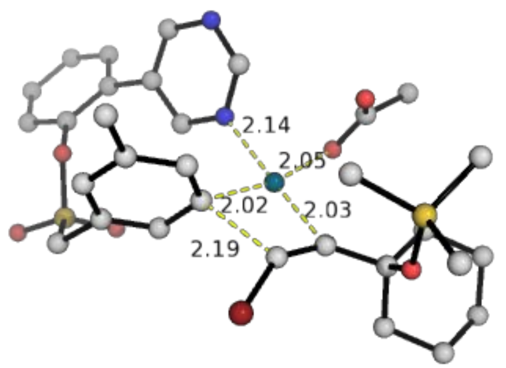	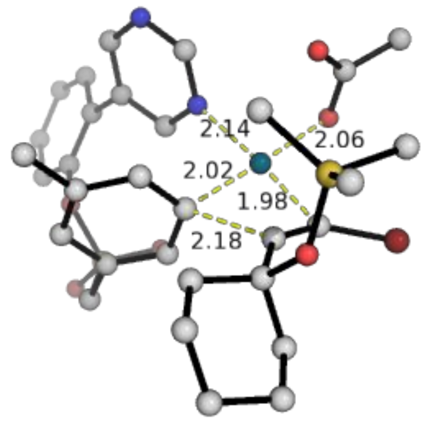
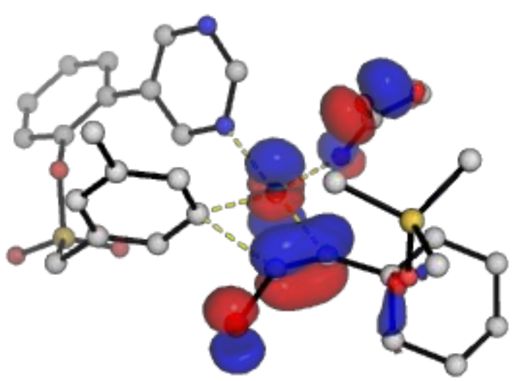	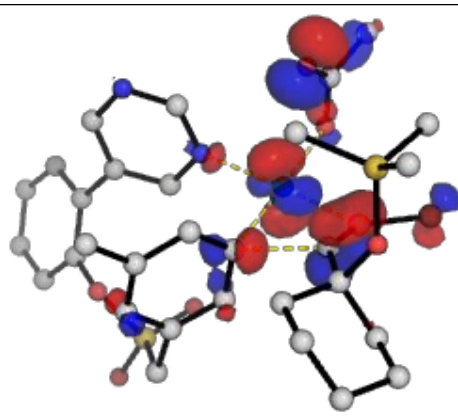

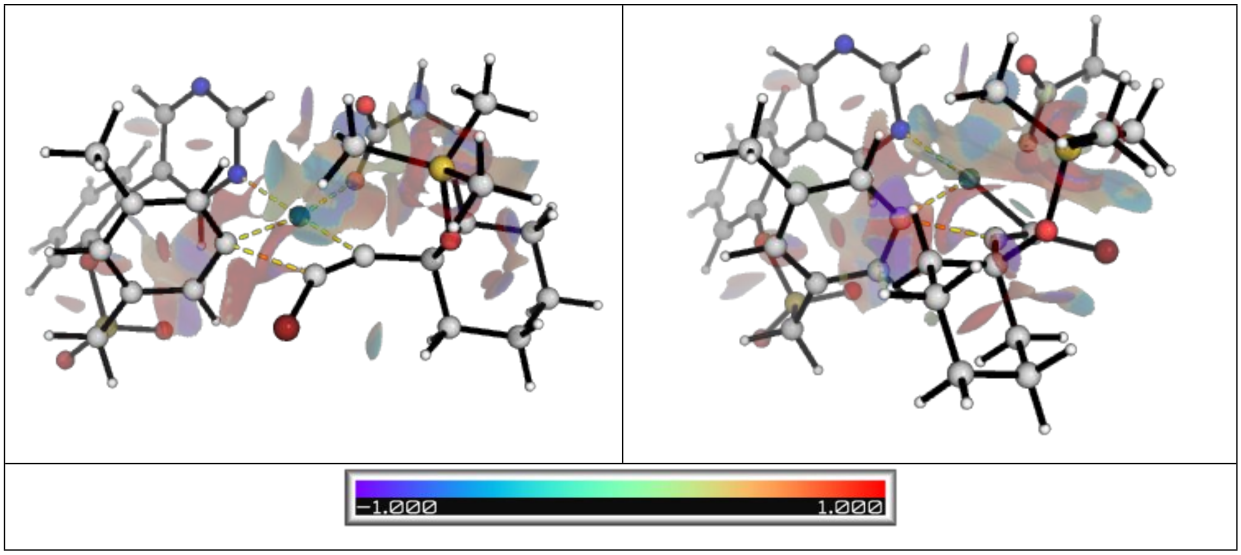

Figure S26. Optimised structures, HOMOs and NCI plots for the regioisomeric 1,2-migratory insertion steps for the siloxy-substituted substrate **1h.**

2.6.14 Comparative study of other arenes with varying substituents

We compared the arene site-selectivity for the other arene substrates used in the present transformation, namely that giving products **4**, **5** and **12**. These substrates differ from substrate **1a** (methyl group on *meta*-position of arene) used in the computational study in that for products **4**, the substituent is *meta*-CF_3; for **5**, it is *meta*-OCF_3 ; for **12**, it is *ortho*-CH_3.

For product **4**, the optimized structures, the HOMO and the NCI plots for the 1,2-migratory insertion step at different arene sites are given in Figure S27. *Meta*-selectivity is favored as for substrate **1a**. Our calculations show that *meta*-functionalization will be favoured by a factor of 10^3, although experimentally, it is favoured only by 7 times. There seems to be a balancing effect between the sterics and electronics for the meta-selectivity, although it is difficult to see the molecular origins from the HOMO and NCI plots.

For product **5**, a similar analysis was performed and the results were shown in Figure S28. Two conformers for the –OCF_3 substituent on the arene can be distinguished, with this group either pointing into or away from the palladacycle. We found that the ones pointing away from the palladacycle has the lower barrier (albeit only slightly), possibly due to more favourable sterics. Once again, for this substrate, the *meta*-functionalization was computationally found to be more favourable than either the *ortho*- or *para*-functionalization.

arene4-ts-3 (*meta-*)	**arene4-ts-3p (*para-*)**	**arene4-ts-3o (*ortho-*)**
ΔG‡ = 14.8‡ (18.3‡)	21.6‡ (21.8‡)	19.9‡ (21.6‡)

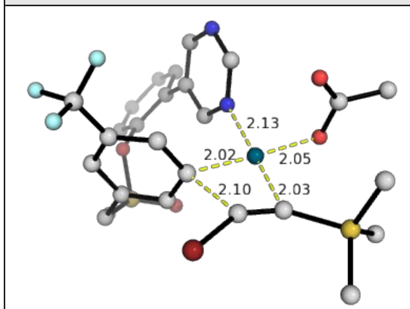

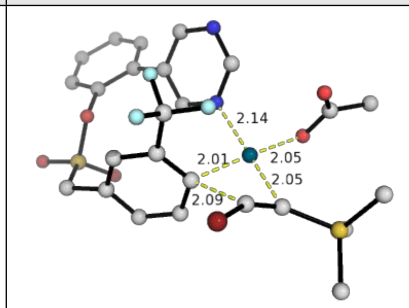

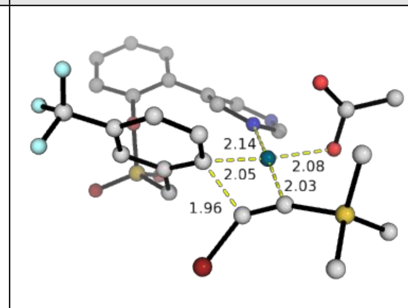

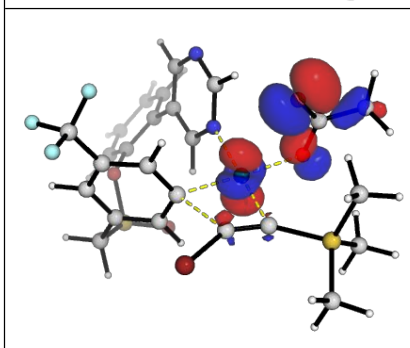

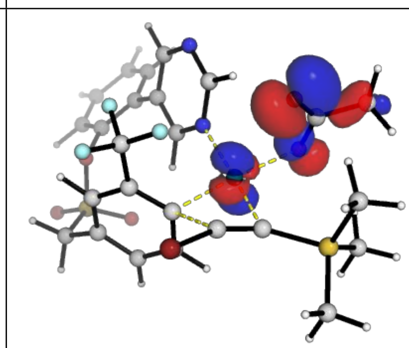

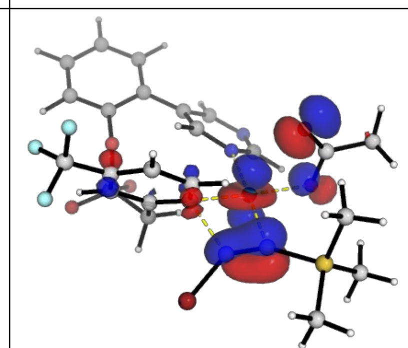

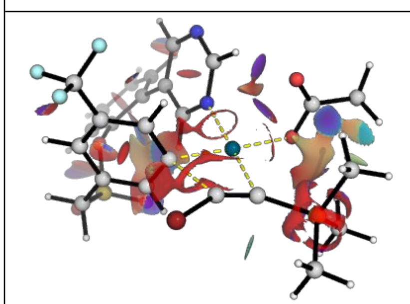

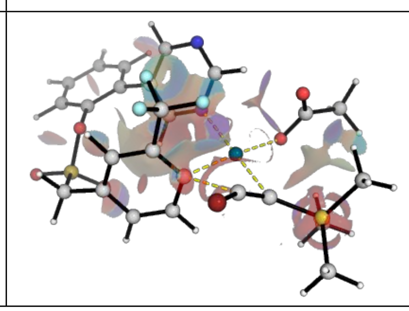

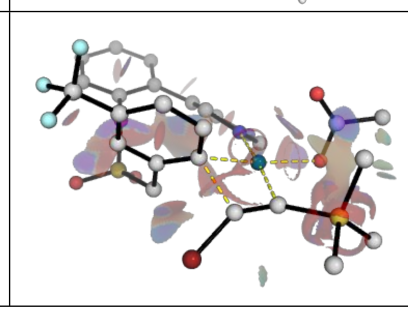

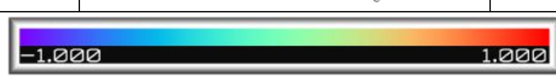

Figure S27. Optimised structures, HOMOs and NCI plots for 1,2-migratory insertion step in site-selectivity studies for arene giving product **4**.

arene5-ts-3-out (*meta-*)	**arene5-ts-3p-out (*para-*)**	**arene5-ts-3o-out (*ortho-*)**
ΔG‡ = 20.3‡ (22.5‡)	23.4‡ (24.1‡)	25.5‡ (26.1‡)
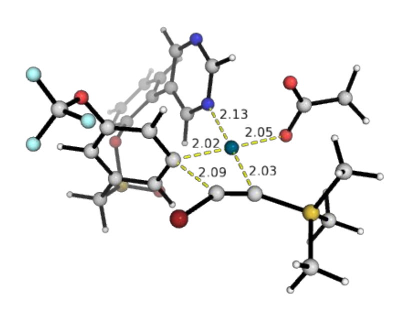	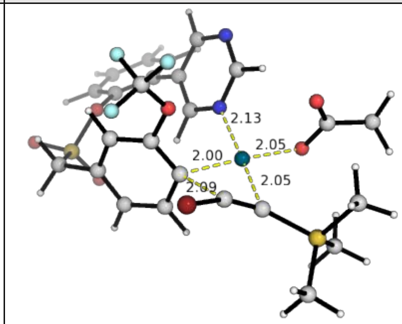	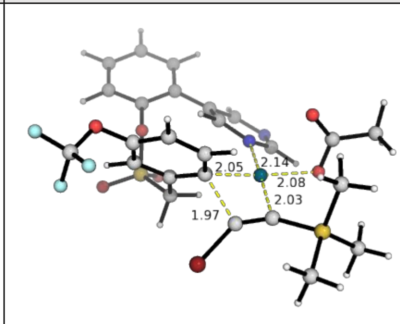
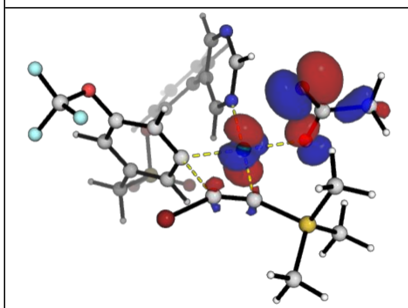	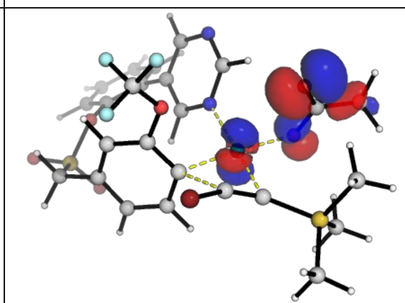	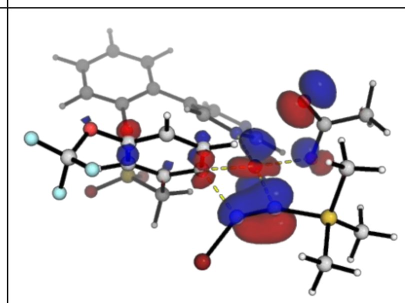
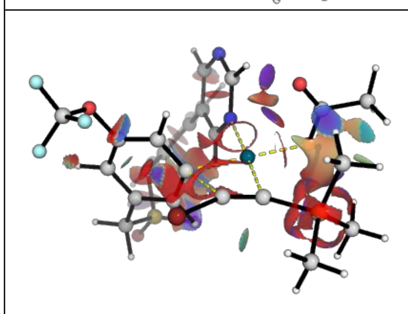	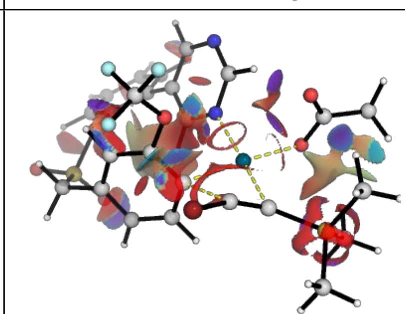	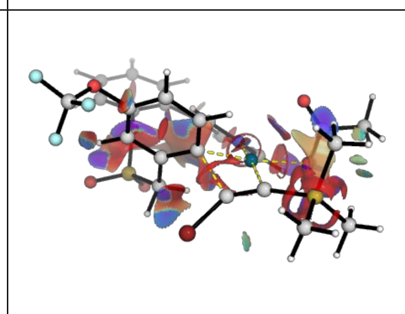
arene5-ts-3-in (*meta-*)	**arene5-ts-3p-in (*para-*)**	**arene5-ts-3o-in (*ortho-*)**
ΔG‡ = 20.9‡ (22.8‡)	24.7‡ (24.6‡)	25.8‡ (26.4‡)
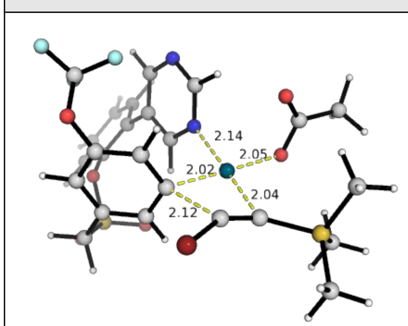	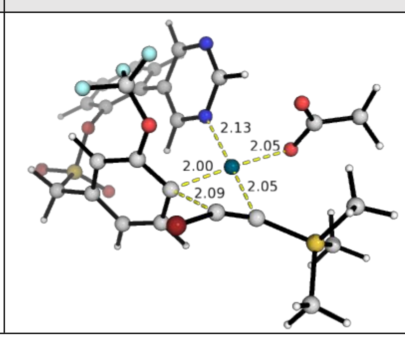	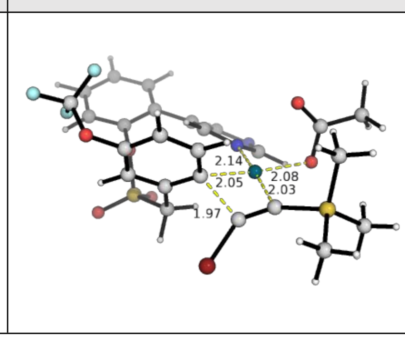

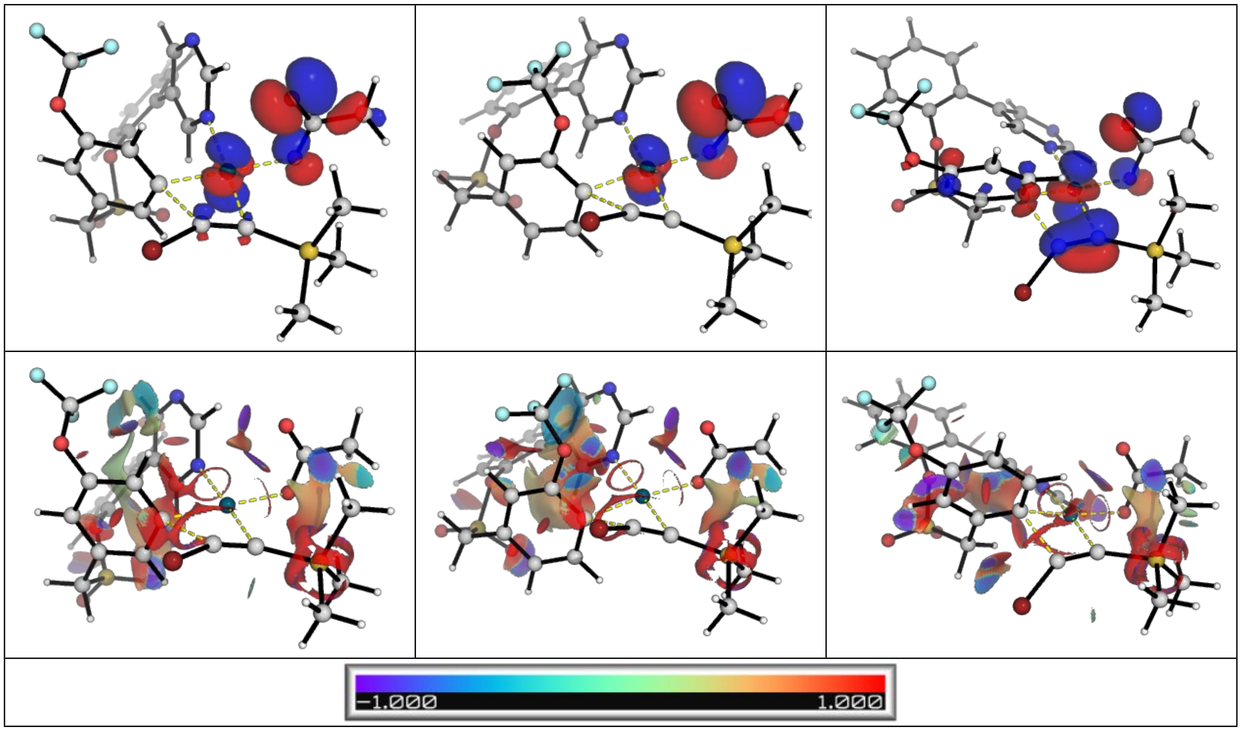

Figure S28. Optimised structures, HOMOs and NCI plots for 1,2-migratory insertion step in site-selectivity studies for arene giving product **5**. The suffix "-out" and "-in" in the TS names indicate the conformation of the –OCF_3 group with respect to the palladacycle.

The results for product **12** is shown in Figure S29. The same *meta*-selectivity is observed, as for substrate **1a**. This is again likely due to the ring strain control in the different membered palladacycle for these TSs. For *meta*- and *para*-functionalization, the TSs have two different conformers with the methyl group on the arene in different orientation. It was found that the TS with the methyl group pointing away from the palladacyclic ring is lower in activation barrier, as would be expected for substrate **1a**.

For all these arene substrates, we have shown that the *meta*-selectivity is obtained in all cases. This shows our computational model of arene site-selectivity via ring strain control by the palladacycle is general and widely applicable to a range of substrates. In addition, it shows that this sterics control is dominant over electronic variations in the substituents in the arene substrates.

arene12-ts-3 (*meta-*)	**arene12-ts-3p (*para-*)**	**arene12-ts-3o (*ortho-*)**
ΔG‡ = 21.9‡ (23.5‡)	24.0‡ (24.9‡)	29.5‡ (28.9‡)
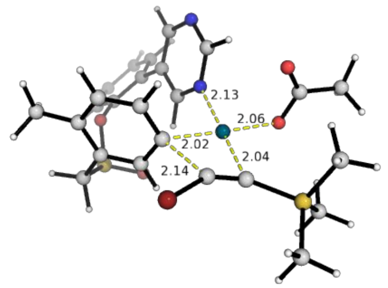	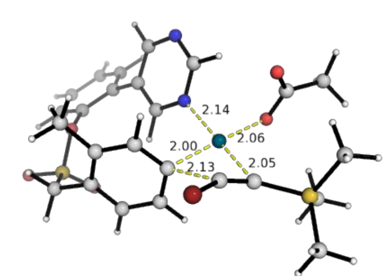	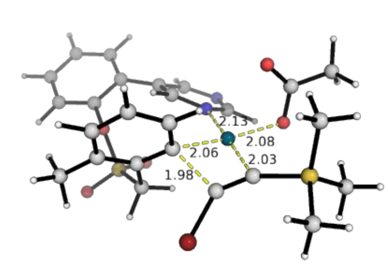
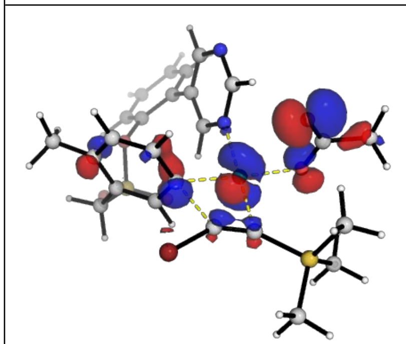	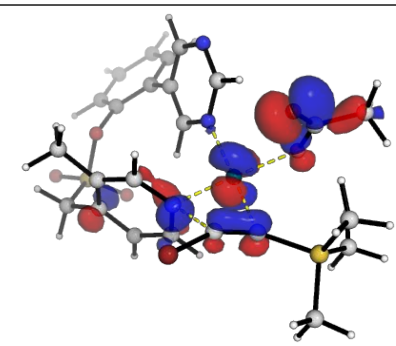	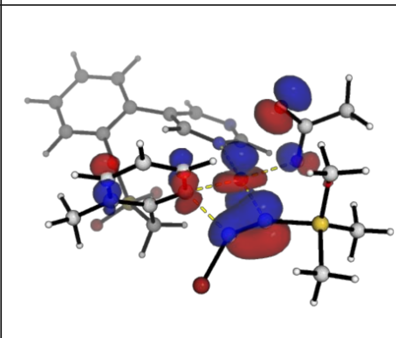
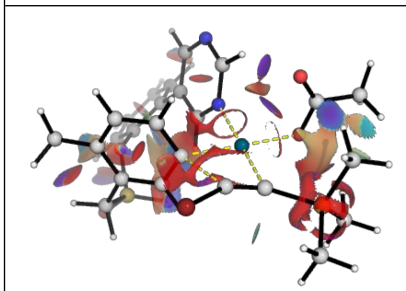	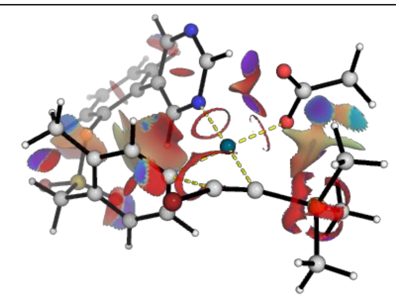	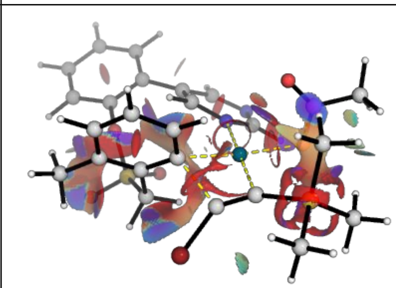
arene12-ts-3-c2 (*meta-*)	**arene12-ts-3p-c2 (*para-*)**	
ΔG‡ = 24.2‡ (24.1‡)	25.6‡ (26.0‡)	
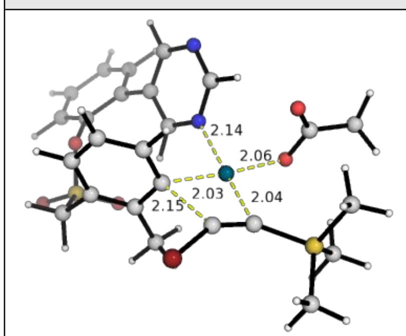	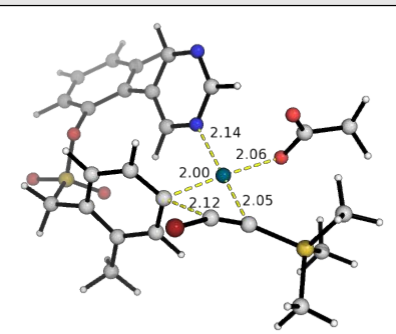	

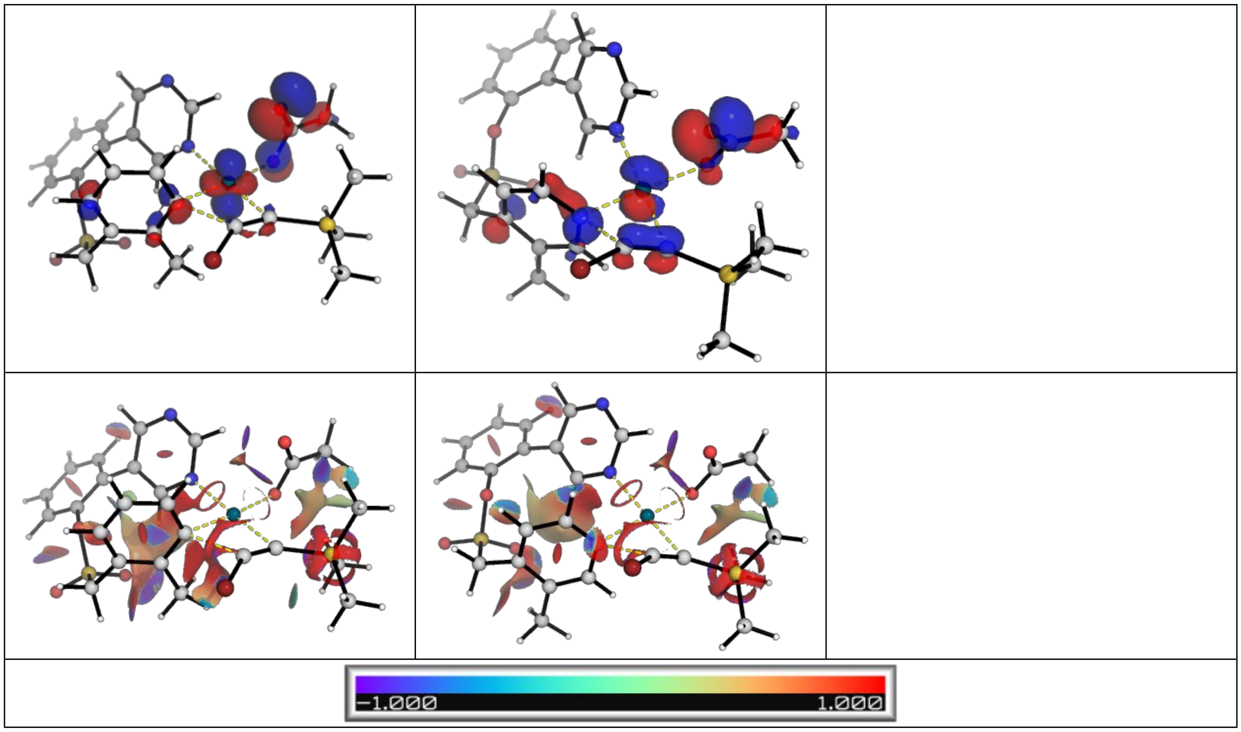

Figure S29. Optimised structures, HOMOs and NCI plots for 1,2-migratory insertion step in site-selectivity studies for arene giving product **12**.

2.6.15 Comparative study of directing group with varying alkyl chain lengths (products 17-19)

Our computational model of site-selectivity control via differing ring strains in the palladacyclic TS predicts that as the length of the directing group increases, this site-selectivity control will diminish. Indeed, this is what was observed experimentally for products **17**, **18** and **19**, that *meta*-selective product formation diminishes. Computationally herein, we show that *meta*-site is favored in the turnover frequency determining 1,2-insertion step for all these substrates. The results are shown in Figure S30. The discrepancy in the quantitative selectivity / product ratio could result from incomplete conformational sampling since with greater chain length in the directing groups, the corresponding possible conformers also increase. Nevertheless, our model successfully predicts selective *meta*-functionalization for all these three substrates.

Product 17		
arene17-ts-3 (*meta*-)	**arene17-ts-3p (*para*-)**	**arene17-ts-3o (*ortho*-)**
ΔG‡ = 19.7‡ (22.0‡)	21.5‡ (21.2‡)	26.8‡ (27.5‡)
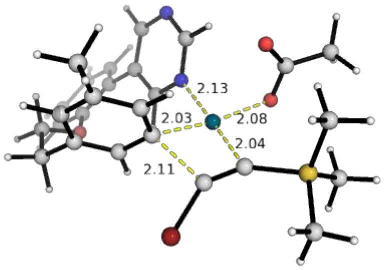	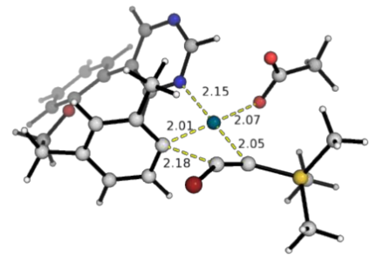	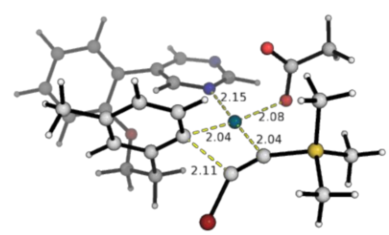
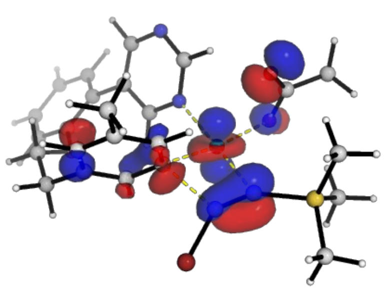	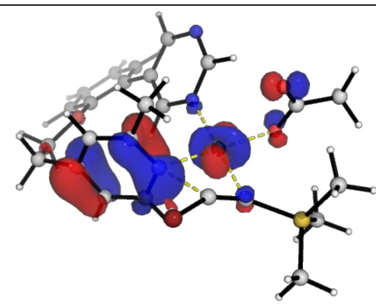	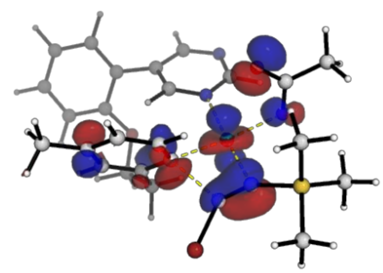
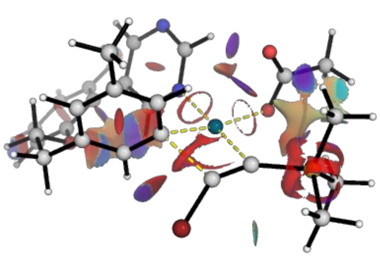	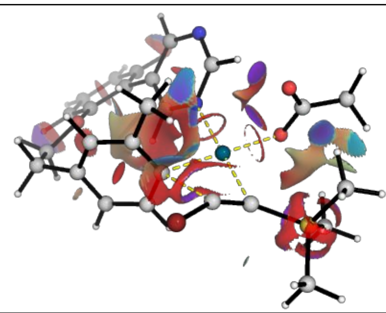	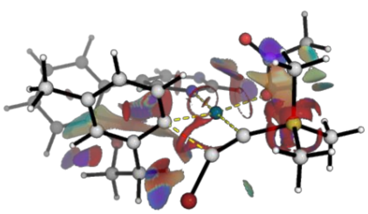
Product 18		
arene18-ts-3 (*meta*-)	**arene18-ts-3p (*para*-)**	**arene18-ts-3o (*ortho*-)**
ΔG‡ = 17.8‡ (19.5‡)	26.5‡ (26.0‡)	19.9‡ (19.9‡)
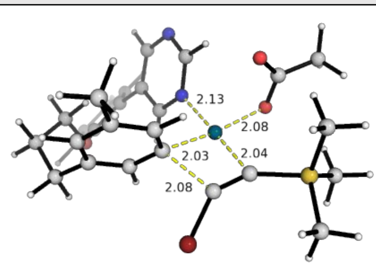	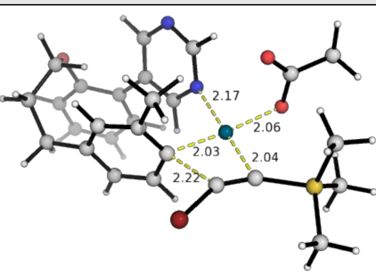	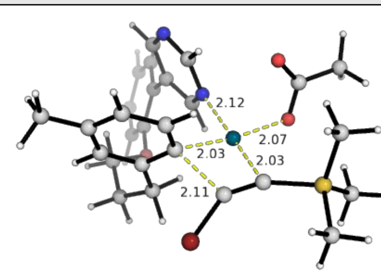

<table>
<tr><td>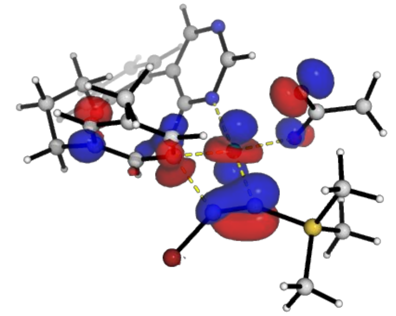</td><td>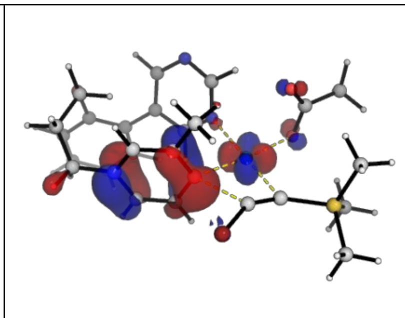</td><td>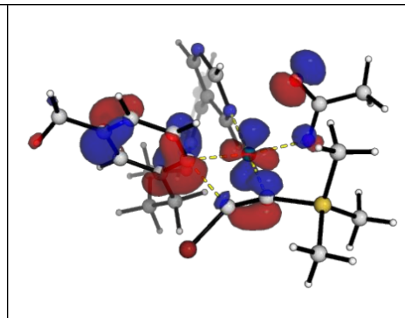</td></tr>
<tr><td>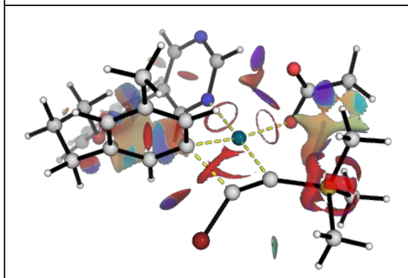</td><td>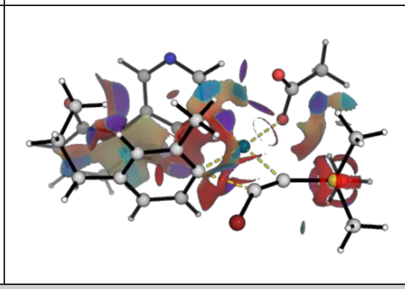</td><td>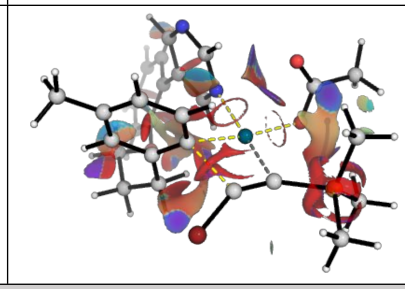</td></tr>
<tr><td colspan="3">Product 19</td></tr>
<tr><td>arene19-ts-3 (meta-)</td><td>arene19-ts-3p (para-)</td><td>arene19-ts-3o (ortho-)</td></tr>
<tr><td>ΔG‡ = 18.1‡ (20.4‡)</td><td>21.1‡ (21.7)</td><td>20.9‡ (21.4‡)</td></tr>
<tr><td>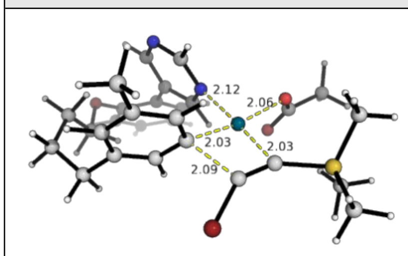
</td><td>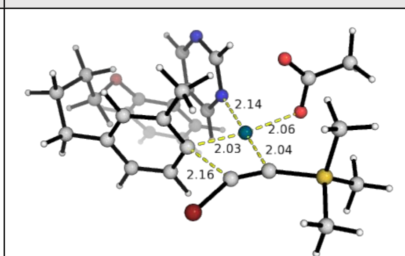
</td><td>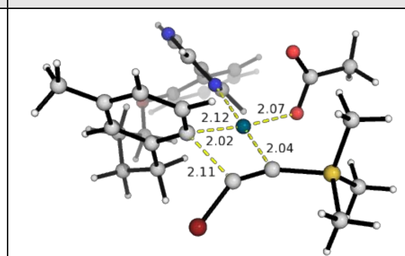
</td></tr>
<tr><td>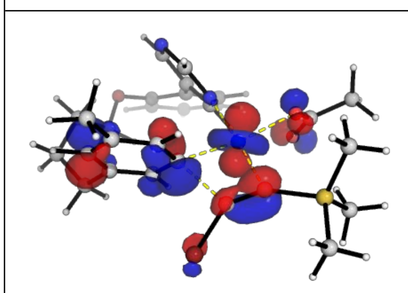</td><td>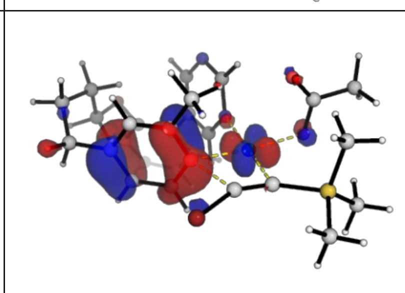</td><td>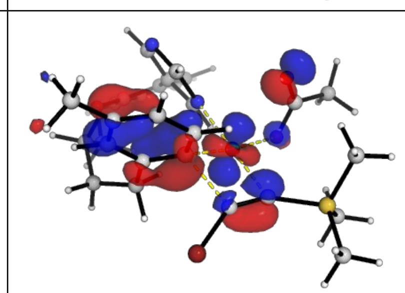</td></tr>
<tr><td>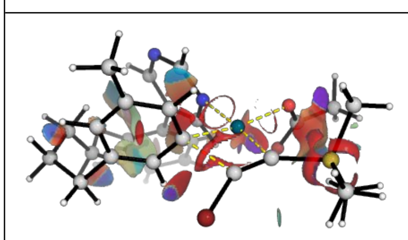</td><td>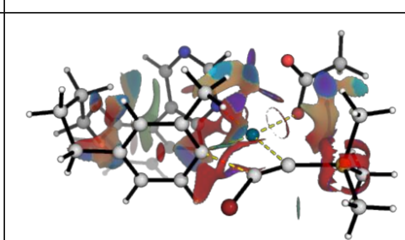</td><td>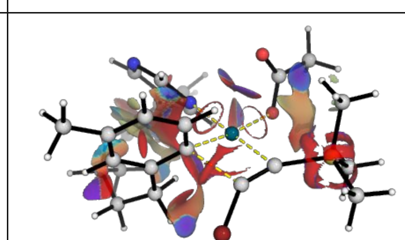</td></tr>
<tr><td colspan="3">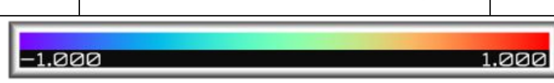
</td></tr>
</table>

Figure S30. Optimised structures, HOMOs and NCI plots for comparison of regioselctivity in product **17-19**.

2.6.16 Absolute energies, zero-point energies

Absolute values (in Hartrees) for SCF energy, zero-point vibrational energy (ZPE), enthalpy and quasi-harmonic Gibbs free energy (at 363K) for optimised structures are given below. Single point corrections in SMD 1,4-dioxane using *ω*B97X-D and MN15 functionals are also included. Each sub-heading corresponds to a subfolder inside the *alkynylation_structures_xyz* folder where all optimised structural coordinates are given in *.xyz* format, along with the corresponding (gas-phase) energy, *E*.

Structure	E/au	ZPE/au	H/au	G/au	qh-G/au	SP *ω*B97X-D (1,4-dioxane)	SP MN15 (1,4-dioxane)
0_sm (starting materials):							
1a	-1426.5229	0.311509	-1426.1822	-1426.271357	-1426.2667	-1429.04845440	-1428.6786329
1b	-3059.2496	0.12121	-3059.1129	-3059.171373	-3059.1703	-3059.73136747	-3059.9403307
1c	-485.35706	0.130012	-485.21303	-485.265131	-485.26489	-486.0681293	-485.9084379
1d	-2881.6333	0.101851	-2881.5201	-2881.570127	-2881.5693	-2882.07267838	-2882.3366382
HOAc	-228.64453	0.062197	-228.57532	-228.611767	-228.61143	-229.13351888	-229.0668662
Nacetylglycine	-436.25343	0.118206	-436.12243	-436.175678	-436.17305	-437.18030569	-437.0523413
HBr	-2575.0853	0.006123	-2575.0752	-2575.098797	-2575.0988	-2574.87712744	-2575.2352612
CuOAc2_monomer	-2096.9448	0.103478	-2096.8259	-2096.887377	-2096.884	-2097.7220570	-2097.862484
CuOAc2_dimer_singlet	-4193.9145	0.2089	-4193.6748	-4193.770684	-4193.7642	-4195.41435355	-4195.7209312
CuOAc2_dimer_triplet	-4193.9647	0.210384	-4193.7241	-4193.819467	-4193.8132	-4195.48133	-4195.770429

CuOAc_dimer_singlet	-3737.8511	0.105272	-3737.7284	-3737.7944	-3737.7912	-3738.42516828	-3738.851
CuOAc_dimer_triplet	-3737.7103	0.104279	-3737.5884	-3737.6552	-3737.6524	-3738.29887073	-3738.7162
CuBr2_monomer	-6789.8301	0.001703	-6789.8214	-6789.860471	-6789.8594	-6789.22792048	-6790.217605
CuBr2_dimer_singlet	-13579.701	0.004317	-13579.682	-13579.74594	-13579.743	-13578.47209	-13580.47502
CuBr2_dimer_triplet	-13579.72	0.003987	-13579.702	-13579.76965	-13579.764	-13578.50789	-13580.49347
AgBr_monomer	-2721.2253	0.000564	-2721.2202	-2721.251781	-2721.2518	-2721.36119518	-2721.3856319
AgBr_dimer	-5442.5245	0.001782	-5442.5131	-5442.563924	-5442.5627	-5442.77059613	-5442.8311465
AgOAc_monomer	-374.7487	0.050645	-374.68909	-374.734768	-374.73318	-375.57469470	-375.1751886
AgOAc_dimer	-749.614	0.104042	-749.49181	-749.561524	-749.55757	-751.22801036	-750.4392581
PdOAc2_trimer	-1751.5873	0.317868	-1751.2239	-1751.355928	-1751.3441	-1755.20433723	-1754.0362117
1_alkynylation_of_1b:							
int-1	-2010.361021	0.417336	-2009.8989	-2010.025439	-2010.0157	-2014.09960593	-2013.3417185
ts-1	-2010.33609	0.411975	-2009.8797	-2010.005994	-2009.9958	-2014.07504621	-2013.3134469

int-2	-2010.35148	0.417256	-2009.8891	-2010.01868	-2010.0072	-2014.0909700	-2013.3314472
int-1'	-1989.299016	0.40982	-1988.8469	-1988.96541	-1988.9582	-1992.99638924	-1992.242002
ts-1'	-1989.285298	0.404477	-1988.8388	-1988.957426	-1988.9496	-1992.98274427	-1992.226918
int-2'	-1989.308364	0.410403	-1988.8556	-1988.975621	-1988.9672	-1993.00391157	-1992.251518
int-3	-4840.971216	0.475881	-4840.4416	-4840.587747	-4840.5761	-4844.70115850	-4844.219901
ts-3	-4840.954399	0.475297	-4840.4262	-4840.571417	-4840.5599	-4844.69041408	-4844.205339
int-4	-4841.020565	0.477956	-4840.49	-4840.632214	-4840.6224	-4844.75555636	-4844.269364
ts-4	-4840.959972	0.476549	-4840.4307	-4840.573444	-4840.5632	-4844.70633991	-4844.221584
int-5	-4841.03872	0.477823	-4840.5075	-4840.652789	-4840.6415	-4844.77052705	-4844.288776
ts-3-c2	-4840.953808	0.475018	-4840.4258	-4840.570625	-4840.5593	-4844.69020998	-4844.205156
ts-4-c2	-4840.959568	0.476335	-4840.4304	-4840.57422	-4840.5633	-4844.70609086	-4844.222823
int-4'	-5215.84045	0.530066	-5215.2484	-5215.412349	-5215.4	-5220.36794079	-5219.492117
ts-4'	-5215.832056	0.529735	-5215.2409	-5215.402897	-5215.3907	-5220.35928688	-5219.483928
int-5'	-5215.865795	0.530375	-5215.2726	-5215.440323	-5215.4261	-5220.4013	-5219.519246
ts-3’z	-5215.75066	0.527466	-5215.1604	-5215.327817	-5215.3139	-5220.28972195	-5219.408864
ts-4'z	-5215.740197	0.526905	-5215.1501	-5215.322905	-5215.3057	-5220.28632879	-5219.406788
int-3r	-4840.966352	0.475466	-4840.4367	-4840.586257	-4840.5731	-4844.70196831	-4844.216596
ts-3r	-4840.95523	0.47543	-4840.4271	-4840.570658	-4840.5596	-4844.69151480	-4844.208097
int-4r	-4841.015859	0.477568	-4840.4854	-4840.629472	-4840.6187	-4844.75055601	-4844.265451
prd-TMS	-1910.712531	0.422586	-1910.2474	-1910.369467	-1910.36	-1913.930509	-1913.409386

1_alkynylation_of_1b (regioconvergence):

int-4r'	-	0.530422	-5215.2395	-5215.405033	-5215.3917	-5220.36410756	-5219.485658

	5215.832104						
ts-4r'	-5215.821896	0.529437	-5215.2308	-5215.394645	-5215.3817	-5220.35427898	-5219.47812
int-5r'	-5215.829729	0.529865	-5215.2374	-5215.403028	-5215.3898	-5220.36688210	-5219.489466
ts-5r'	-5215.800846	0.528577	-5215.2093	-5215.37938	-5215.3637	-5220.34501888	-5219.467047
int-6r'	-5215.871336	0.530833	-5215.2777	-5215.445362	-5215.4312	-5220.40546946	-5219.525982
2_alkynylation_of_1b_aa_ligand:							
ts-1'a	-1989.241518	0.404846	-1988.7947	-1988.914288	-1988.9057	-1992.93996133	-1992.185971
ts-1'b	-2217.946095	0.468797	-2217.4274	-2217.567499	-2217.5552	-2222.12071512	-2221.297634
ts-1'c	-2217.950755	0.467665	-2217.4326	-2217.575045	-2217.5616	-2222.1295546	-2221.3056348
ts3'a	-5048.547111	0.531403	-5047.9573	-5048.114495	-5048.1014	-5052.71629339	-5052.172854
ts3'b	-5048.564282	0.531205	-5047.9743	-5048.134568	-5048.1203	-5052.74047130	-5052.192636
ts3'c	-5048.571284	0.532029	-5047.9809	-5048.13779	-5048.1249	-5052.74364579	-5052.196485
3_alkynylation_of_1b_copper:							
prd-TMS-Cu	-4007.706141	0.528899	-4007.1194	-4007.27282	-4007.2619	-4011.68135651	-4011.302816
int-5'-Cu	-6728.989054	0.529306	-6728.3963	-6728.565912	-6728.5517	-6733.07561264	-6732.724159
ts-4'-Cu	-6937.993403	0.582236	-6937.3431	-6937.519912	-6937.5065	-6942.47112391	-6942.135956
ts-5r'-Cu	-6937.944999	0.581394	-6937.2949	-6937.474663	-6937.4599	-6942.43658511	-6942.099334
ts-4'-Cu-I	-6709.9488	0.529478	-6709.3577	-6709.5201	-6709.508	-6713.95378711	-6713.688
ts-5r'-Cu-I	-6709.9194	0.530303	-6709.3274	-6709.4906	-6709.4778	-6713.94078388	-6713.6704
4_arene_site_selectivity_ortho_para:							

ts-1o	-2010.327235	0.412335	-2009.8706	-2009.996525	-2009.9864	-2014.06251681	-2013.3048429
ts-1'o	-1989.275333	0.40504	-1988.8284	-1988.945718	-1988.9386	-1992.97006819	-1992.21543
ts-3o	-4840.950848	0.475039	-4840.4227	-4840.567922	-4840.5564	-4844.68267726	-4844.2002067
int-4o	-4841.005502	0.478328	-4840.4746	-4840.615898	-4840.6066	-4844.73707307	-4844.253322
ts-1p	-2010.335874	0.412169	-2009.8794	-2010.004978	-2009.9953	-2014.07305762	-2013.3139172
ts-1'p	-1989.285331	0.405046	-1988.8386	-1988.955232	-1988.9485	-1992.97998020	-1992.2270019
ts-3p	-4840.95513	0.47566	-4840.4269	-4840.568977	-4840.5592	-4844.68772197	-4844.2061858
int-4p	-4841.014183	0.478097	-4840.4835	-4840.625278	-4840.6157	-4844.74520831	-4844.2619844
pyridine	-247.762761	0.089473	-247.66632	-247.703094	-247.7031	-248.30299639	-248.2171106
ts-3-iso	-5088.733157	0.565521	-5088.1063	-5088.273417	-5088.2574	-5093.00230034	-5092.431749
ts-3o-iso	-5088.739269	0.566537	-5088.1119	-5088.273959	-5088.2602	-5093.00429760	-5092.43484
ts-3p-iso	-5088.737798	0.566374	-5088.1105	-5088.27522	-5088.2607	-5093.00522025	-5092.437843
5_alternative_oxidative_addition_TSs:							
ts-3-oa-c1	-4840.926859	0.475106	-4840.3986	-4840.542395	-4840.5316	-4844.65853300	-4844.176038
ts-3-oa-c2	-4840.916281	0.474524	-4840.3882	-4840.535615	-4840.5231	-4844.65155100	-4844.168891
ts-3-oa-c3	-4840.920333	0.475375	-4840.3919	-4840.536547	-4840.5252	-4844.65176600	-4844.169894
ts-3-oa-c4	-4840.913291	0.475415	-4840.3848	-4840.530401	-4840.5186	-4844.64899900	-4844.166361
6_ethynyltrimethylsilane_1c:							
ts-3H	-2267.064352	0.484575	-2266.5286	-2266.667859	-2266.6578	-2271.02940120	-2270.174764
int-4H	-2267.117887	0.487514	-2266.5796	-2266.716169	-2266.7075	-2271.08034834	-2270.225851

ts-4H	-2267.065965	0.485481	-2266.5297	-2266.667975	-2266.6581	-2271.03263981	-2270.176345
int-5H	-2267.080525	0.486262	-2266.5432	-2266.682216	-2266.6722	-2271.04173857	-2270.19011
ts-5H	-2267.058347	0.482448	-2266.5243	-2266.666613	-2266.655	-2271.02464274	-2270.168419
int-6H	-2267.112587	0.487541	-2266.5733	-2266.716186	-2266.7043	-2271.07262933	-2270.218973
ts-3rH	-2267.059619	0.484192	-2266.5242	-2266.663393	-2266.653	-2271.02667613	-2270.173159
int-4rH	-2267.110337	0.487008	-2266.5722	-2266.71284	-2266.7017	-2271.07618079	-2270.220442
7_bromoethynylbenzene_1d:							
int-3P	-4663.348539	0.45632	-4662.8422	-4662.982617	-4662.97	-4667.04108395	-4666.611194
ts-3P	-4663.334882	0.455895	-4662.8302	-4662.966822	-4662.9556	-4667.02770871	-4666.598967
int-4P	-4663.410381	0.458554	-4662.9032	-4663.037486	-4663.0277	-4667.10511821	-4666.673142
int-4'P	-5038.220005	0.511025	-5037.6508	-5037.806846	-5037.7944	-5042.70847151	-5041.885059
ts-4'P	-5038.213948	0.50998	-5037.6461	-5037.802513	-5037.7894	-5042.70363654	-5041.881219
int-5'P	-5038.246678	0.510894	-5037.677	-5037.836798	-5037.8225	-5042.73960204	-5041.913369
int-3rP	-4663.348567	0.456396	-4662.8424	-4662.981827	-4662.9697	-4667.03983832	-4666.610208
ts-3rP	-4663.334352	0.45606	-4662.8295	-4662.965766	-4662.9546	-4667.02827091	-4666.599432
int-4rP	-4663.408013	0.458631	-4662.9007	-4663.035552	-4663.0254	-4667.10120678	-4666.670752
int-4r'P	-5038.221148	0.51122	-5037.6518	-5037.809372	-5037.796	-5042.71271368	-5041.888975
ts-4r'P	-5038.203812	0.510319	-5037.6359	-5037.791775	-5037.7788	-5042.69533863	-5041.873737
int-5r'P	-5038.208472	0.51074	-5037.6393	-5037.798524	-5037.7844	-5042.70482600	-5041.88134

ts-5r'P	-5038.179023	0.508913	-5037.6113	-5037.773914	-5037.7576	-5042.68075194	-5041.853769
int-6r'P	-5038.253672	0.510711	-5037.6836	-5037.846764	-5037.8306	-5042.74558486	-5041.921402
Pd-1d2-c1	-5890.364189	0.205082	-5890.1328	-5890.219516	-5890.2141	-5891.64277896	-5891.906803
Pd-1d2-c2	-5890.359886	0.205108	-5890.1286	-5890.218338	-5890.2113	-5891.62582953	-5891.89701
Pd-1b2-c1	-6245.565123	0.242534	-6245.2867	-6245.39694	-6245.3888	-6246.93689409	-6247.085401
Pd-1b2-c2	-6245.56809	0.242148	-6245.292	-6245.39765	-6245.3897	-6246.92986787	-6247.081794
8_other_substrates:							
1e	-3294.59	0.292704	-3294.2712	-3294.3534	-3294.35	-3295.634897	-3295.721341
1e-ts-3	-5076.2974	0.646681	-5075.5873	-5075.7523	-5075.7398	-5080.593801	-5079.986219
1e-int-4	-5076.3526	0.649515	-5075.64	-5075.803	-5075.7916	-5080.645143	-5080.03672
1e-ts-4'	-5451.1723	0.70129	-5450.3991	-5450.5815	-5450.5684	-5456.261713	-5455.261447
1e-int-5'	-5451.2102	0.702589	-5450.4347	-5450.6222	-5450.6067	-5456.308062	-5455.301817
1e-ts-3r	-5076.2924	0.64712	-5075.5819	-5075.7473	-5075.7345	-5080.591088	-5079.983186
1e-int-4r	-5076.3522	0.649212	-5075.6394	-5075.8049	-5075.7925	-5080.649833	-5080.040274
1e-ts-5r'	-5451.1408	0.700775	-5450.3667	-5450.5561	-5450.5398	-5456.2458	-5455.243674
1f	-3176.924	0.205792	-3176.6972	-3176.7683	-3176.7656	-3177.686636	-3177.835616
1f-ts-3	-4958.6302	0.559899	-4958.0119	-4958.1676	-4958.1552	-4962.645778	-4962.101901
1f-ts-3r	-4958.6289	0.560226	-4958.0107	-4958.1647	-4958.1529	-4962.645048	-4962.101922
1f-int-4r	-4958.6908	0.562524	-4958.0702	-4958.2244	-4958.2128	-4962.705875	-4962.160724
1f-ts-5r'	-5333.4774	0.613627	-5332.7958	-5332.9756	-5332.9591	-5338.298815	-5337.362075
1g	-3176.9162	0.207853	-3176.6874	-3176.7601	-3176.7565	-3177.680792	-3177.827112
1g-ts-3	-4958.624	0.561729	-4958.0041	-4958.1605	-4958.1475	-4962.640979	-4962.093565

1g-ts-3r	-4958.6197	0.562476	-4957.9995	-4958.1535	-4958.1419	-4962.638822	-4962.092373
1g-int-4r	-4958.6825	0.564508	-4958.0601	-4958.2153	-4958.203	-4962.699377	-4962.151008
1g-ts-5r'	-5333.4697	0.615664	-5332.7861	-5332.9672	-5332.9502	-5338.294293	-5337.354334
1h	-3368.5384	0.275855	-3368.2375	-3368.3177	-3368.3143	-3369.708772	-3369.79762
1h-ts-3	-5150.2455	0.631166	-5149.5526	-5149.7138	-5149.7016	-5154.666852	-5154.061617
1h-ts-3r	-5150.2426	0.630357	-5149.5501	-5149.7127	-5149.6998	-5154.663669	-5154.058248
rct4	-1723.7941	0.290043	-1723.4729	-1723.5664	-1723.5616	-1726.834042	-1726.446171
arene4-ts-3	-5138.2315	0.453342	-5137.7229	-5137.8746	-5137.8618	-5142.486279	-5141.979126
arene4-ts-3o	-5138.2273	0.453186	-5137.7188	-5137.8705	-5137.8577	-5142.478066	-5141.973756
arene4-ts-3p	-5138.2327	0.45348	-5137.7243	-5137.8715	-5137.8611	-5142.47737	-5141.975429
rct5	-1798.8924	0.294448	-1798.5655	-1798.6645	-1798.6575	-1802.07487	-1801.676443
arene5-ts-3 -in	-5213.3278	0.45795	-5212.8135	-5212.9666	-5212.9538	-5217.719327	-5217.204019
arene5-ts-3-out	-5213.3268	0.457935	-5212.8125	-5212.9672	-5212.9537	-5217.71939	-5217.203736
arene5--ts-3o-in	-5213.3225	0.457925	-5212.8082	-5212.9611	-5212.9484	-5217.711578	-5217.198451
arene5-ts-3o-out	-5213.3222	0.457813	-5212.808	-5212.962	-5212.9488	-5217.711411	-5217.198334
arene5-ts-3p-in	-5213.3285	0.458439	-5212.8141	-5212.9645	-5212.9532	-5217.71457	-5217.202591
arene5-ts-3p-out	-5213.3269	0.458125	-5212.8125	-5212.9665	-5212.9533	-5217.714939	-5217.201559
rct12	-1426.5206	0.311768	-1426.1798	-1426.2688	-1426.264	-1429.045799	-1428.678001

arene1 2-ts-3	-4840.9551	0.475883	-4840.4268	-4840.5694	-4840.5591	-4844.688978	-4844.204842
arene1 2-ts-3 -c2	-4840.9558	0.476203	-4840.4273	-4840.568	-4840.5587	-4844.686417	-4844.205075
arene1 2-ts-3p	-4840.9516	0.475861	-4840.4233	-4840.5655	-4840.5554	-4844.685907	-4844.202936
arene1 2-ts-3p-c2	-4840.951	0.475834	-4840.4228	-4840.5643	-4840.5545	-4844.683508	-4844.201388
arene1 2-ts-3o	-4840.9485	0.475274	-4840.4206	-4840.5627	-4840.5527	-4844.676657	-4844.196173
rct17	-917.69754	0.329967	-917.34115	-917.42361	-917.41975	-919.6751142	-919.3624192
arene1 7-ts-3	-4332.1279	0.493298	-4331.584	-4331.7241	-4331.713	-4335.319402	-4334.889262
arene1 7-ts-3o	-4332.1213	0.493222	-4331.5775	-4331.7169	-4331.7061	-4335.308496	-4334.881006
arene1 7-ts-3p	-4332.1323	0.494036	-4331.5882	-4331.7242	-4331.7154	-4335.318613	-4334.892731
rct18	-956.91929	0.358325	-956.53275	-956.61915	-956.61514	-958.991959	-958.6575218
arene1 8-ts-3	-4371.3551	0.52194	-4370.781	-4370.9237	-4370.9127	-4374.640464	-4374.189512
arene1 8-ts-3o	-4371.3554	0.521749	-4370.7814	-4370.924	-4370.9132	-4374.636954	-4374.188736
arene1 8-ts-3p	-4371.3496	0.522566	-4370.7754	-4370.9147	-4370.9054	-4374.62844	-4374.181094
rct19	-996.14608	0.38758	-995.72869	-995.81932	-995.81428	-998.3137032	-997.9588521
arene1 9-ts-3	-4410.5805	0.55009	-4409.9763	-4410.1237	-4410.1118	-4413.960342	-4413.488137
arene1 9-ts-3o	-4410.5796	0.550033	-4409.9755	-4410.1217	-4410.1105	-4413.956386	-4413.486858
arene1 9-ts-3p	-4410.5823	0.55073	-4409.978	-4410.1224	-4410.1122	-4413.957052	-4413.487479

2.6.17 Optimised geometries

All optimized geometries (in .xyz format with their associated energy in Hartrees) are included in a separate folder named *alkynylation_structures_xyz* with an associated README file. All these data have been uploaded to zenodo.org (DOI:10.5281/zenodo.3550223) and are freely available.

3. References:

Full reference for Gaussian 16 software:

Gaussian 16, Revision A.01, Frisch, M. J., Trucks, G. W., Schlegel, H. B., Scuseria, G. E., Robb, M. A., Cheeseman, J. R., Scalmani, G., Barone, V., Mennucci, B., Petersson, G. A., Nakatsuji, H., Caricato, M., Li, X., Hratchian, H. P., Izmaylov, A. F., Bloino, J., Zheng, G., Sonnenberg, J. L., Hada, M., Ehara, M., Toyota, K., Fukuda, R., Hasegawa, J., Ishida, M., Nakajima, T., Honda, Y., Kitao, O., Nakai, H., Vreven, T., Montgomery Jr., J. A.; Peralta, J. E., Ogliaro, F., Bearpark, M., Heyd, J. J., Brothers, E., Kudin, K. N., Staroverov, V. N., Kobayashi, R., Normand, J., Raghavachari, K., Rendell, A., Burant, J. C., Iyengar, S. S., Tomasi, J., Cossi, M., Rega, N., Millam, J. M., Klene, M., Knox, J. E., Cross, J. B., Bakken, V., Adamo, C., Jaramillo, J., Gomperts, R., Stratmann, R. E., Yazyev, O., Austin, A. J., Cammi, R., Pomelli, C., Ochterski, J. W., Martin, R. L., Morokuma, K., Zakrzewski, V. G., Voth, G. A., Salvador, P., Dannenberg, J. J., Dapprich, S., Daniels, A. D., Farkas, Ö., Foresman, J. B., Ortiz, J. V, Cioslowski, J., Fox, D. J. Gaussian, Inc. & Wallingford CT. (2016).

(1) Bag, S., Jayarajan, R., Mondal, R. & Maiti, D. Template-assisted *meta*-C–H alkylation and alkenylation of arenes. *Angew. Chem. Int. Ed.* **56**, 3182-3186 (2017).

(2) Bag, S., Jayarajan, R., Dutta, U., Chowdhury, R., Mondal, R. & Maiti, D. Remote *meta*-C–H cyanation of arenes enabled by a pyrimidine based auxiliary. *Angew. Chem. Int. Ed.* **56**, 12538-12542 (2017).

(3) Jayarajan, R., Das, J., Bag, S., Chowdhury, R. & Maiti, D. Diverse *meta*-C–H functionalization of arenes across different linker lengths. *Angew. Chem. Int. Ed.* **57**, 7659 –7663 (2018).

(4) Bera, M., Maji, A., Sahoo, S.K. & Maiti, D. Palladium(II)-catalyzed *meta*-C−H olefination: constructing multisubstituted arenes through homo-diolefination and sequential hetero-diolefination. *Angew. Chem. Int. Ed.* **54**, 8515 –8519 (2015).

(5) Griffith, W. P., Shoair, A. G. & Suriaatmaja, M. Ruthenium-catalysed cleavage of alkenes and alkynes to carboxylic acids. *Synth. Commun.* **30**, 3091-3095 (2000).

(6) Xu, G., Hartman, T. L., Wargo, H., Turpin, J. A., Buckheit, R.W. & Cushman, M. Synthesis of alkenyldiarylmethane (ADAM) non-nucleoside HIV-1 reverse transcriptase inhibitors with non-identical aromatic rings. *Bioorg. Med Chem*. **10**, 283-90 (2002).

(7) Himo, F., Lovell, T., Hilgraf, R., Rostovtsev. V. V., Noodleman, L., Sharpless, K. B. & Fokin, V. V. Copper(I)-catalyzed synthesis of azoles. DFT study predicts unprecedented reactivity and intermediates. *J. Am. Chem. Soc.* **127**, 210 –216 (2005).

(1) Rappoport, D.; Furche, F. Property-Optimized Gaussian Basis Sets for Molecular Response Calculations. *J. Chem. Phys.* **2010**, *133* (13), 134105.

(2) Andrae, D.; Häußermann, U.; Dolg, M.; Stoll, H.; Preuß, H. Energy-Adjustedab Initio Pseudopotentials for the Second and Third Row Transition Elements. *Theor. Chim. Acta* **1990**, *77* (2), 123–141.

(3) Weigend, F.; Ahlrichs, R. Balanced Basis Sets of Split Valence, Triple Zeta Valence and Quadruple Zeta Valence Quality for H to Rn: Design and Assessment of Accuracy. *Phys. Chem. Chem. Phys.* **2005**, *7* (18), 3297–3305.

(4) Weigend, F. Accurate Coulomb-Fitting Basis Sets for H to Rn. *Phys. Chem. Chem. Phys.* **2006**, *8* (9), 1057–1065.

(5) Guin, S.; Dolui, P.; Zhang, X.; Paul, S.; Singh, V. K.; Pradhan, S.; Chandrashekar, H. B.; Anjana, S. S.; Paton, R. S.; Maiti, D. Iterative Arylation of Amino Acids and Aliphatic Amines via δ-C(Sp 3)−H Activation: Experimental and Computational Exploration. *Angew. Chemie - Int. Ed.* **2019**, *58* (17), 5633–5638.

(6) Landstrom, E. B.; Handa, S.; Aue, D. H.; Gallou, F.; Lipshutz, B. H. EvanPhos: A Ligand for Ppm Level Pd-Catalyzed Suzuki–Miyaura Couplings in Either Organic

Solvent or Water. *Green Chem.* **2018**, *20* (15), 3436–3443.

(7) Dandu, N. K.; Reed, J. A.; Odoh, S. O. Performance of Density Functional Theory for Predicting Methane-to-Methanol Conversion by a Tri-Copper Complex. *J. Phys. Chem. C* **2018**, *122* (2), 1024–1036.

(8) Zhou, T.; Malakar, S.; Webb, S. L.; Krogh-Jespersen, K.; Goldman, A. S. Polar Molecules Catalyze CO Insertion into Metal-Alkyl Bonds through the Displacement of an Agostic C-H Bond. *Proc. Natl. Acad. Sci. U. S. A.* **2019**, *116* (9), 3419–3424.

(9) Luconi, L.; Demirci, U. B.; Peruzzini, M.; Giambastiani, G.; Rossin, A. Ammonia Borane and Hydrazine Bis(Borane) Dehydrogenation Mediated by an Unsymmetrical (PNN) Ruthenium Pincer Hydride: Metal–Ligand Cooperation for Hydrogen Production. *Sustain. Energy Fuels* **2019**.

(10) Achar, T. K.; Zhang, X.; Mondal, R.; Shanavas, M. S.; Maiti, S.; Maity, S.; Pal, N.; Paton, R. S.; Maiti, D. Palladium-Catalyzed Directed Meta -Selective C−H Allylation of Arenes: Unactivated Internal Olefins as Allyl Surrogates. *Angew. Chemie Int. Ed.* **2019**, *58*, 2–10.

(11) Fukui, K. Formulation of the Reaction Coordinate. *J. Phys. Chem.* **2005**, *74* (23), 4161–4163.

(12) Fukui, K. The Path of Chemical Reactions - The IRC Approach. *Acc. Chem. Res.* **1981**, *14* (12), 363–368.

(13) Grimme, S. Supramolecular Binding Thermodynamics by Dispersion-Corrected Density Functional Theory. *Chem. - A Eur. J.* **2012**, *18* (32), 9955–9964.

(14) Funes-Ardoiz, I.; Paton, R. S. GoodVibes v1.0.1 http://doi.org/10.5281/zenodo.56091.

(15) Sosa, C.; Andzelm, J.; Elkin, B. C.; Wimmer, E.; Dobbs, K. D.; Dixon, D. A. A Local Density Functional Study of the Structure and Vibrational Frequencies of Molecular Transition-Metal Compounds. *J. Phys. Chem.* **1992**, *96* (16), 6630–6636.

(16) Godbout, N.; Salahub, D. R.; Andzelm, J.; Wimmer, E. Optimization of Gaussian-Type Basis Sets for Local Spin Density Functional Calculations. Part I. Boron through

Neon, Optimization Technique and Validation. *Can. J. Chem.* **1992**, *70* (2), 560–571.

(17) Dang, Y.; Qu, S.; Nelson, J. W.; Pham, H. D.; Wang, Z. X.; Wang, X. The Mechanism of a Ligand-Promoted C(Sp3)-H Activation and Arylation Reaction via Palladium Catalysis: Theoretical Demonstration of a Pd(II)/Pd(IV) Redox Manifold. *J. Am. Chem. Soc.* **2015**, *137* (5), 2006–2014.

(18) Weibel, J.-M.; Blanc, A.; Pale, P. Ag-Mediated Reactions: Coupling and Heterocyclization Reactions. *Chem. Rev.* **2008**, *108* (8), 3149–3173.

(19) Daugulis, O.; Do, H. Q.; Shabashov, D. Palladium- and Copper-Catalyzed Arylation of Carbon-Hydrogen Bonds. *Acc. Chem. Res.* **2009**, *42* (8), 1074–1086.

(20) Chen, X.; Engle, K. M.; Wang, D. H.; Jin-Quan, Y. Palladium(II)-CataIyzed C-H Aetivation/C-C Cross-Coupling Reactions: Versatility and Practicality. *Angew. Chemie - Int. Ed.* **2009**, *48* (28), 5094–5115.

(21) Lyons, T. W.; Sanford, M. S. Palladium-Catalyzed Ligand-Directed C−H Functionalization Reactions. *Chem. Rev.* **2010**, *110* (2), 1147–1169.

(22) Lotz, M. D.; Camasso, N. M.; Canty, A. J.; Sanford, M. S. Role of Silver Salts in Palladium-Catalyzed Arene and Heteroarene C-H Functionalization Reactions. *Organometallics* **2017**, *36* (1), 165–171.

(23) Masui, K.; Ikegami, H.; Mori, A. Palladium-Catalyzed C-H Homocoupling of Thiophenes: Facile Construction of Bithiophene Structure. *J. Am. Chem. Soc.* **2004**, *126* (16), 5074–5075.

(24) Stuart, D. R.; Villemure, E.; Fagnou, K. Elements of Regiocontrol in Palladium-Catalyzed Oxidative Arene Cross-Coupling. *J. Am. Chem. Soc.* **2007**, *129* (40), 12072–12073.

(25) Hull, K. L.; Sanford, M. S. Catalytic and Highly Regioselective Cross-Coupling of Aromatic C-H Substrates. *J. Am. Chem. Soc.* **2007**, *129* (39), 11904–11905.

(26) Potavathri, S.; Dumas, A. S.; Dwight, T. A.; Naumiec, G. R.; Hammann, J. M.; DeBoef, B. Oxidant-Controlled Regioselectivity in the Oxidative Arylation of N-

Acetylindoles. *Tetrahedron Lett.* **2008**, *49* (25), 4050–4053.

(27) Anand, M.; Sunoj, R. B.; Schaefer, H. F. Non-Innocent Additives in a Palladium(II)-Catalyzed C–H Bond Activation Reaction: Insights into Multimetallic Active Catalysts. *J. Am. Chem. Soc.* **2014**, *136* (15), 5535–5538.

(28) Li, H.; Liu, J.; Sun, C. L.; Li, B. J.; Shi, Z. J. Palladium-Catalyzed Cross-Coupling of Polyfluoroarenes with Simple Arenes. *Org. Lett.* **2011**, *13* (2), 276–279.

(29) Wang, G. W.; Zhou, A. X.; Li, S. X.; Yang, S. D. Regio- and Stereoselective Allylic C-H Arylation with Electron-Deficient Arenes by 1,1′-Bi-2-Naphthol-Palladium Cooperation. *Org. Lett.* **2014**, *16* (11), 3118–3121.

(30) Preciado, S.; Mendive-Tapia, L.; Albericio, F.; Lavilla, R. Synthesis of C-2 Arylated Tryptophan Amino Acids and Related Compounds through Palladium-Catalyzed C-H Activation. *J. Org. Chem.* **2013**, *78* (16), 8129–8135.

(31) Paramonov, S. E.; Mychlo, E. V.; Troyanov, S. I.; Kuz'mina, N. P. Synthesis and Thermal Stability of Silver Carboxylates: Crystal Structure of Silver Pivalate. *Russ. J. Inorg. Chem.* **2000**, *45* (12), 1852–1856.

(32) Olson, L. P.; Whitcomb, D. R.; Rajeswaran, M.; Blanton, T. N.; Stwertka, B. J. The Simple yet Elusive Crystal Structure of Silver Acetate and the Role of the Ag - Ag Bond in the Formation of Silver Nanoparticles during the Thermally Induced Reduction of Silver Carboxylates. *Chem. Mater.* **2006**, *18* (6), 1667–1674.

(33) Schmidbaur, H.; Schier, A. Argentophilic Interactions. *Angew. Chemie - Int. Ed.* **2015**, *54* (3), 746–784.

(34) Taguchi, H.; Miyashita, H.; Tsubouchi, A.; Takeda, T. First Anionic Silyl Migration from Sp2 Carbon to Carbonyl Oxygen. Stereospecific Allylation of (Z)-β-Trimethylsilyl-α,β-Unsaturated Ketones. *Chem. Commun.* **2002**, *2* (19), 2218–2219.

(35) Tsubouchi, A.; Sasaki, N.; Enatsu, S.; Takeda, T. Regio- and Stereoselective Preparation of (Z)-Silyl Enol Ethers by Three-Component Coupling Using α,β-Unsaturated Acylsilanes as Core Building Blocks. *Tetrahedron Lett.* **2013**, *54* (10), 1264–1267.

(36) Tsubouchi, A.; Matsuda, H.; Kira, T.; Takeda, T. Silyl Migration in Conjunction with Substitution on Silicon in Copper(I) t -Butoxide-Promoted Coupling between o -Silylphenyl Ketones and Organic Halides. *Chem. Lett.* **2009**, *38* (12), 1180–1181.

(37) Wheeler, S. E.; Houk, K. N.; Schleyer, P. V. R.; Allen, W. D. A Hierarchy of Homodesmotic Reactions for Thermochemistry. *J. Am. Chem. Soc.* **2009**, *131* (7), 2547–2560.

(38) Wheeler, S. E. Homodesmotic Reactions for Thermochemistry. *Wiley Interdiscip. Rev. Comput. Mol. Sci.* **2012**, *2* (2), 204–220.

(39) Zhang, X.; Lu, G.; Sun, M.; Mahankali, M.; Ma, Y.; Zhang, M.; Hua, W.; Hu, Y.; Wang, Q.; Chen, J.; et al. A General Strategy for Synthesis of Cyclophane-Braced Peptide Macrocycles via Palladium-Catalysed Intramolecular Sp 3 C-H Arylation. *Nat. Chem.* **2018**, *10* (5), 540–548.

(40) Holganza, M. K.; Trigoura, L.; Elfarra, S.; Seo, Y.; Oiler, J.; Xing, Y. Copper (II) Catalyzed Homocoupling and Heterocoupling of Terminal Alkynes. *Tetrahedron Lett.* **2019**, *60* (17), 1179–1181.

(41) Bai, R.; Zhang, G.; Yi, H.; Huang, Z.; Qi, X.; Liu, C.; Miller, J. T.; Kropf, A. J.; Bunel, E. E.; Lan, Y.; et al. Cu(II)-Cu(I) Synergistic Cooperation to Lead the Alkyne C-H Activation. *J. Am. Chem. Soc.* **2014**, *136* (48), 16760–16763.

(42) Zuidema, E.; Bolm, C. Sub-Mol % Catalyst Loading and Ligand-Acceleration in the Coppercatalyzed Coupling of Aryl Iodides and Terminal Alkyenes. *Chem. - A Eur. J.* **2010**, *16* (14), 4181–4185.

(43) Zou, L. H.; Johansson, A. J.; Zuidema, E.; Bolm, C. Mechanistic Insights into Copper-Catalyzed Sonogashira-Hagihara-Type Cross-Coupling Reactions: Sub-Mol % Catalyst Loadings and Ligand Effects. *Chem. - A Eur. J.* **2013**, *19* (25), 8144–8152.

(44) He, C.; Ke, J.; Xu, H.; Lei, A. Synergistic Catalysis in the Sonogashira Coupling Reaction: Quantitative Kinetic Investigation of Transmetalation. *Angew. Chemie - Int. Ed.* **2013**, *52* (5), 1527–1530.

(45) Zhang, G.; Yi, H.; Zhang, G.; Deng, Y.; Bai, R.; Zhang, H.; Miller, J. T.; Kropf, A. J.;

Bunel, E. E.; Lei, A. Direct Observation of Reduction of Cu(II) to Cu(I) by Terminal Alkynes. *J. Am. Chem. Soc.* **2014**, *136* (3), 924–926.

(46) Shimizu, T.; Morisako, S.; Yamamoto, Y.; Kawachi, A. 1,2-Silyl Migration in 1-Halonaphthalenes Catalyzed by I 2. *Heteroat. Chem.* **2018**, *29* (4), e21434.

(47) Barczak, N. T.; Rooke, D. A.; Menard, Z. A.; Ferreira, E. M. Stereoselective Synthesis of Tetrasubstituted Olefins through a Halogen-Induced 1,2-Silyl Migration. *Angew. Chemie Int. Ed.* **2013**, *52* (29), 7579–7582.

(48) Zhao, R.; Zhang, R. Q. A New Insight into π-π Stacking Involving Remarkable Orbital Interactions. *Phys. Chem. Chem. Phys.* **2016**, *18* (36), 25452–25457.

(49) Zhao, R.; Zhang, R. Q. Intermolecular Orbital Interaction in π Systems. *Mol. Phys.* **2018**, *116* (7–8), 978–986.

(50) Neel, A. J.; Hilton, M. J.; Sigman, M. S.; Toste, F. D. Exploiting Non-Covalent π Interactions for Catalyst Design. *Nature* **2017**, *543* (7647), 637–646.

(51) Yamada, S. Cation-π Interactions in Organic Synthesis. *Chem. Rev.* **2018**, *118* (23), 11353–11432.

(52) Xi, P.; Yang, F.; Qin, S.; Zhao, D.; Lan, J.; Gao, G.; Hu, C.; You, J. Palladium(II)-Catalyzed Oxidative C-H/C-H Cross-Coupling of Heteroarenes. *J. Am. Chem. Soc.* **2010**, *132* (6), 1822–1824.

(53) Martínez, Á. M.; Alonso, I.; Rodríguez, N.; Gómez Arrayás, R.; Carretero, J. C. Rhodium-Catalyzed Copper-Assisted Intermolecular Domino C−H Annulation of 1,3-Diynes with Picolinamides: Access to Pentacyclic Π-Extended Systems. *Chem. – A Eur. J.* **2019**, *25* (22), 5733–5742.

(54) Funes-Ardoiz, I.; Maseras, F. Computational Characterization of the Mechanism for the Oxidative Coupling of Benzoic Acid and Alkynes by Rhodium/Copper and Rhodium/Silver Systems. *Chem. - A Eur. J.* **2018**, *24* (47), 12383–12388.

(55) Funes-Ardoiz, I.; Maseras, F. Cooperative Reductive Elimination: The Missing Piece in the Oxidative-Coupling Mechanistic Puzzle. *Angew. Chemie - Int. Ed.* **2016**, *55* (8),

2764–2767.

(56) Usui, K.; Haines, B. E.; Musaev, D. G.; Sarpong, R. Understanding Regiodivergence in a Pd(II)-Mediated Site-Selective C-H Alkynylation. *ACS Catal.* **2018**, *8* (5), 4516–4527.